

Nonconvex weighted variational metal artifacts removal via convergent primal-dual algorithms

Lianfang Wang¹, Zhangling Chen¹, Zhifang Liu¹, Yutong Li¹,
Yunsong Zhao², Hongwei Li², and Huibin Chang^{1‡}

¹ School of Mathematical Sciences, Tianjin Normal University, Tianjin, 300387, China

² School of Mathematical Sciences, Capital Normal University, Beijing, 100048, China

E-mail: changhuibin@gmail.com

Abstract. Direct reconstruction through filtered back projection engenders metal artifacts in polychromatic computed tomography images, attributed to highly attenuating implants, which further poses great challenges for subsequent image analysis. Inpainting the metal trace directly in the Radon domain for the extant variational method leads to strong edge diffusion and potential inherent artifacts. With normalization based on pre-segmentation, the inpainted outcome can be notably ameliorated. However, its reconstructive fidelity is heavily contingent on the precision of the pre-segmentation, and highly accurate segmentation of images with metal artifacts is non-trivial in actuality. In this paper, we propose a nonconvex weighted variational approach for metal artifact reduction. Specifically, in lieu of employing a binary function with zeros in the metal trace, an adaptive weight function is designed in the Radon domain, with zeros in the overlapping regions of multiple disjoint metals as well as areas of highly attenuated projections, and the inverse square root of the measured projection in other regions. A nonconvex $L^1 - \alpha L^2$ regularization term is incorporated to further enhance edge contrast, alongside a box-constraint in the image domain. Efficient first-order primal-dual algorithms, proven to be globally convergent and of low computational cost owing to the closed-form solution of all subproblems, are devised to resolve such a constrained nonconvex model. Both simulated and real experiments are conducted with comparisons to other variational algorithms, validating the superiority of the presented method. Especially in comparison to Reweighted JSR, our proposed algorithm can curtail the total computational cost to at most one-third, and for the case of inaccurate pre-segmentation, the recovery outcomes by the proposed algorithms are notably enhanced.

Keywords: computerized tomography, metal artifact reduction, nonconvex regularization, primal-dual hybrid gradient algorithm.

‡ Corresponding author.

1 Introduction

X-ray computed tomography (CT) is one of the most common means of medical diagnosis. However, when metallic implants present, the reconstructed CT images by conventional reconstruction algorithms like the filtered back projection (FBP) [1] and simultaneous algebraic reconstruction technique [2] may suffer from serious metal artifacts, thus potentially engendering misdiagnoses. Consequently, conceiving efficacious methodologies for metallic artifact reduction (MAR) is imperative.

One effective approach is to modify the model by incorporating imaging physics [3, 4, 5, 6, 7]. This methodology can mitigate artifacts whilst preserving boundaries and specifics. However, under conditions of elevated noise levels, a divergence transpires betwixt the aforementioned modelling and the authentic model, inevitably engendering unsatisfactory outcomes. Another well-known way is to identify the metal-affected projection as missing data and use interpolation to recover it. [Some are to directly inpaint the domain with different interpolation algorithms \[8, 9, 10, 11, 12\], leading to inaccurate boundaries and the introduction of new artifacts.](#) In order to enhance the performance [13, 14], Meyer et al. [13] later proposed a normalized metal artifact reduction (NMAR), which utilized prior information to normalize the measurement and then interpolated the sinogram of the metal region. Interpolation alone cannot precisely restore the true missing projection, and thus still introduce new artifacts. With the remarkable success of deep learning in medical image processing, recent studies have implemented deep neural networks (DNNs) to tackle the problem of reducing metal artifacts. [The existing researches consist of the image-to-image learning \[15, 16, 17, 18, 19\], the sinogram domain network \[20, 21, 22, 23, 24\] and dual domain \(both the image and sinogram domains\) \[25, 26, 27, 28, 29\] that utilizes either residual learning or adversarial learning techniques.](#) However, DNNs commonly require large, representative training datasets and extensive computational resources, imposing practical limitations on their widespread adoption.

As a critical mathematical technique for MAR, variational regularization methods offer interpretability, stability, and computational efficiency with modest local resource requirements. Since the correction process involves solving a mathematically ill-posed problem, regularization-based methods play a crucial role. [Successful examples include the total variation \(TV\) \[30, 31, 32, 33\] and the wavelet frame-based approach \[34, 35, 36, 37\]. Furthermore, different variants of TV regularization methods \[38, 39, 40, 41, 42\] have been presented in order to achieve more accurate reconstruction.](#) Due to the non-uniformity of metal artifacts, modelling solely based on uncontaminated projection information and regularization may not be sufficient for effectively removing metal artifacts. Therefore, many researchers proposed incorporating preprocessed images into the reconstruction process. For instance, Zhang, Dong and Liu [36] proposed to normalize the original data in the sinogram domain by projections of pre-segmentation. Then an effective iterative reconstruction was obtained relying on the regularization on dual domains.

The existing methods directly inpainted the metal trace (the regions related to the metal in the sinogram domain) [43, 44, 33], which were acknowledged to produce strong diffusion around the metal (See Fig. 4(b)), and even new artifacts (See Fig. 4(d)). Other methods further normalized the Radon domain [13, 36] based on the projection of a segmentation, which required relatively accurate pre-segmentation. However, it is also challenging to segment the CT images contaminated by metal artifacts. Furthermore, the convex regularization models, either with TV or tight frames, were prone to a reduction of the edge contrast [45]. In this paper, in lieu of employing a binary function with zeros in the metal trace, an adaptive weight function in the Radon domain is designed, with zeros in the overlapping region of multiple separated metals as well as the area of high attenuated projections, and the inverse square root of the measured projection in other regions. To further enhance the edge contrast, a nonconvex $L^1 - \alpha L^2$ regularization term is considered, such that we develop a non-convex weighted variational method for MAR, together with a box-constraint in the image domain. To resolve such a constrained non-convex model, we reformulate the proposed model into saddle-point problems based on the predual forms of TV. We then design efficient first-order primal-dual algorithms that are proven to be globally convergent under mild conditions. In both the simulated and real experiments, compared with other existing methods, such as beam-hardening corrector (BCMAR) [3], NMAR [13], [inpainting with compound prior modelling both sinogram and image sparsity \(TV-TV inpainting\)](#) [44] and [the reweighted joint spatial-Radon domain \(Reweighted JSR \)](#) [36], the proposed algorithms produce higher accuracy reconstruction with low computational cost.

The main contributions of this paper are listed as follows:

- We present a novel weighted nonconvex variational model to correct metal artifacts by combining the nonconvex regularization with an adaptive weighted norm. Namely, the weight function is specially constructed based on the hybrid scheme utilizing the measured projection other than simply setting it to a binary matrix.
- We develop a first-order preconditioned primal-dual hybrid gradient algorithm to solve the reformulated penalized saddle-point problem for the proposed model, proving its convergence given proper parameters. Then by introducing an auxiliary variable in the Radon domain, an even faster fully-splitting primal-dual hybrid gradient algorithm is further proposed, now with guaranteed convergence under the additional assumption that the auxiliary variable is bounded. Both proposed algorithms can be efficiently implemented, as each subproblem has a closed-form solution.
- We conduct numerous experiments to evaluate the various aspects including convergence, parameter impact and performance for the proposed algorithms. Numerically, the proposed methods can produce competitive results in terms of peak signal-to-noise ratio (PSNR) and structural similarity index measure (SSIM), among all the compared variational methods. Especially, for less precise pre-segmentation, the proposed algorithms can reconstruct significantly superior result

in comparison to Reweighted JSR. Moreover, the proposed fully splitting variant algorithm with much faster convergence, can reduce the total computational cost to at most one-third than Reweighted JSR.

The remainder of the paper is organized as follows. In section 2, we briefly review some of the basic concepts involved. The nonconvex weighted MAR model with a box-constraint is presented, and the efficient splitting algorithms are given in section 3, with the convergence guarantee in section 4. In section 5, the effectiveness of the proposed algorithm is validated by numerous experiments. Section 6 summarizes this work.

2 Preliminaries

2.1 Polychromatic X-ray CT and related variational reconstruction methods

For a multichromatic energy X-ray, the adoption of the monochromatic energy assumption allows the imaging model to be rewritten as

$$\mathcal{P}u \approx Y, \tag{2.1}$$

where Y is the measured projection data, $\mathcal{P} : X \rightarrow \mathbb{R}^{m_1 \times m_2}$ is the Radon transform representing the discrete line integrals at m_1 different projection angles and along a total of m_2 different beams and $u \in X = \mathbb{R}^{n \times n}$ denotes the target image at a specific but unknown energy level. Components with high attenuation have greater energy dependence, such as metal implants, and therefore, solving (2.1) leads to severe artifacts that greatly reduce the image quality.

By introducing TV regularization in the projection domain, one can treat the metal trace as missing data and try to recover it via the following model [44]

$$\min_f \frac{1}{2} \|B_\Omega^c \odot (f - Y)\|^2 + \lambda \|\nabla f\|_1, \tag{2.2}$$

where for all $1 \leq i \leq m_1, 1 \leq j \leq m_2$, $(B_\Omega^c)_{i,j} := 1 - (B_\Omega)_{i,j}$ with B_Ω being a binary matrix related to metal trace Ω defined as follows

$$(B_\Omega)_{i,j} := \begin{cases} 0 & \text{if } (i, j) \in \Omega, \\ 1 & \text{otherwise,} \end{cases}$$

the notations \odot , $\|\cdot\|$ and ∇ denote the Hadamard product, the standard Frobenius norm in $\mathbb{R}^{m_1 \times m_2}$ and the gradient operator, respectively, and the norm $\|\cdot\|_1$ is defined as:

$$\|p\|_1 := \sum_{1 \leq i,j \leq n} |(p_x)_{i,j}| + |(p_y)_{i,j}| \quad \forall p = (p_x, p_y) \in X \times X.$$

After arriving at the projection data by solving the above model, the final reconstruction is immediately derived by FBP. Similarly, one can directly consider the sparse restoration in the image domain via the following TV-MAR [29] model

$$\min_u \frac{1}{2} \|B_\Omega^c \odot (\mathcal{P}u - Y)\|^2 + \lambda \|\nabla u\|_{2,1}. \tag{2.3}$$

where the norm $\|\cdot\|_{2,1}$ is defined as

$$\|p\|_{2,1} := \sum_{1 \leq i,j \leq n} \sqrt{|(p_x)_{i,j}|^2 + |(p_y)_{i,j}|^2} \quad \forall p \in X \times X.$$

They have good performance in suppressing artifacts and noises, but the textures in the image may be erased.

Subsequently, in order to balance detail preservation and artifact reduction, Zhang, Dong and Liu [36] considered a dual domain model

$$\begin{aligned} \min_{u,f} \frac{1}{2} \|\mathcal{P}u - Y_s f\|^2 + \|\boldsymbol{\lambda}_1 \cdot W_1 u\|_{1,2} + \|\boldsymbol{\lambda}_2 \cdot W_2 f\|_{1,2} \\ + \frac{1}{2} \|B_\Omega^c \odot (f - Y/Y_s)\|^2, \end{aligned}$$

where Y_s is the Radon transform of a pre-segmentation based on the level set method (the level set method [46] is used to obtain segmentation including low-density components (soft tissues) and high-density components such as bones and metals),

$$\|\boldsymbol{\lambda}_i \cdot W_i u\|_{1,2} = \left\| \sum_s \left(\sum_l \boldsymbol{\lambda}_{i(l,s)} |(W_i u)_{l,s}|^2 \right)^{\frac{1}{2}} \right\|_1 \quad \forall i = 1, 2$$

with $\boldsymbol{\lambda}_i > 0$ and W_i , $i = 1, 2$ being tight wavelet frames, and “/” denotes dot division of two matrices. Although the MAR results are greatly improved, such a method highly relies on the accuracy of the pre-segmentation.

2.2 Anisotropic-isotropic regularization

Variational methods with TV [47] can preserve edge information for piecewise-constant images. In order to enhance the sparsity, one may consider the L^0 pseudo-norm of the image gradient $\|\nabla u\|_0$. However, directly solving the minimization using such a norm is NP-hard, and its nonconvex approximation is a better alternative. A typical example is the weighted anisotropic and isotropic TV (AITV)

$$\text{AITV}(u) := \|\nabla u\|_1 - \alpha \|\nabla u\|_{2,1}.$$

It has been widely used in image processing [39, 48, 49], which produces recovery results with better contrast and fruitful details compared to traditional TV.

3 The proposed variational method for MAR

In this section, we propose a new nonconvex weighted model with a box-constraint to reduce metal artifacts produced by polychromatic X-ray imaging systems and develop effective convergent algorithms. Since the pixel value of the digital image is finite, the box constraint is reasonable. Especially for CT images, the pixel value represents the attenuation coefficient in a particular case [50] in practice. In fact, the box-constraint has also been widely used in image denoising [51], image classification [52] and CT reconstruction [49].

3.1 A nonconvex weighted MAR with a box-constraint

A non-convex weighted model with a box-constraint can be given below

$$\min_u \frac{1}{2\lambda} \|W \odot (\mathcal{P}u - Y)\|^2 + \|\nabla u\|_1 - \alpha \|\nabla u\|_{2,1} \quad \text{s.t. } u \in [0, c], \quad (3.1)$$

where the constant c is the upper bound of the reconstructed image, λ and α are two positive parameters,

$$W := \frac{1_{m_1, m_2}}{\max\{Y^{\frac{1}{2}}, \varepsilon 1_{m_1, m_2}\}} \odot B_{\Omega_t}, \quad (3.2)$$

where $1_{m_1, m_2} \in \mathbb{R}^{m_1 \times m_2}$ denotes the all-ones matrix, \div , and $\max\{\cdot, \cdot\}$ denote the elementwise division and maximum of two matrices, respectively. As expressed in (3.2), the parameter ε serves to preclude division by zero.

Here

$$\Omega_t := O_m \cup O_t$$

is a subset of the metal trace Ω , where O_m represents the projection region jointly through each two separated metals (as shown in the red box area in Figure 1(a)), and the region for highly attenuated projections

$$O_t := \{(i, j) \in \Omega \mid Y_{i,j} \geq t \times \|Y\|_{\max} \quad \forall 1 \leq i \leq m_1, 1 \leq j \leq m_2\}$$

with thresholding level t and $\|Y\|_{\max} := \max_{(\hat{i}, \hat{j}) \in \{1, 2, \dots, m_1\} \times \{1, 2, \dots, m_2\}} |Y_{\hat{i}, \hat{j}}|$.

In (3.1), the weighted fidelity term W makes the recovery mechanism more efficient. If only the non-metallic information of the projection data is considered (i.e. use B_{Ω}^c as the weighted matrix instead of W) as (2.2), the boundary in the image domain may be diffused, and new artifacts also appear (as shown in Figure 4(d)). That may be caused by discarding too many projections in the metal trace. Hence, we here propose to only discard the most severely contaminated projections, which are either the intersection of two metals as O_m or the region O_t related to other relatively high attenuation materials (e.g. bones). Moreover, an inverse square root of the measured projections is combined as (3.2) in order to adaptively balance the error distribution, i.e. bigger errors in the Radon domain are allowed for the higher attenuated projections.

In addition, we show how to determine the region O_m . A rough reconstruction is obtained by FBP or using the conjugate gradient (CG) method by solving the following least-square problem

$$\min_u \frac{1}{2} \|\mathcal{P}u - Y\|^2. \quad (3.3)$$

The reconstructed image, denoted by u_a , is shown in Figure 1(b). And then the position of the metal in the image domain can be obtained by simple threshold processing. Further the different metals are projected separately to get the overlap area O_m .

To better demonstrate the proposed CT image reconstruction method for reducing metal artifacts, we summarize the entire procedure in the flowchart shown in Figure 2.

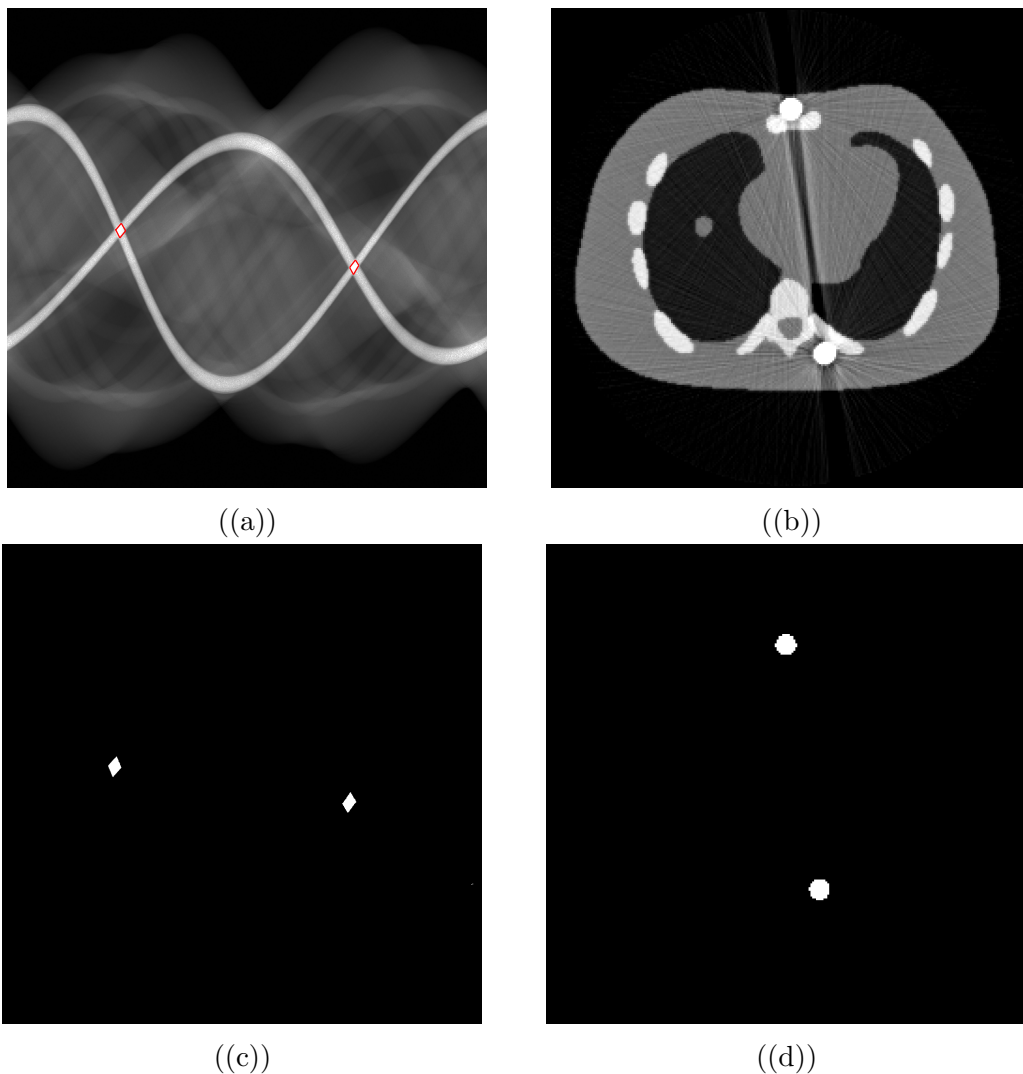


Figure 1: (a) The measured projection data. (b) The reconstructed image u_a by the analysis model (3.3) (4600 Hounsfield Units (HU) window, 1300 HU level). (c) The overlap area Ω_t . (d) The metal image.

3.2 Primal-dual optimization for the penalized model

Due to the nonconvex regularization, (3.1) is a nonconvex optimization problem. A classical approach for solving such non-convex model is to use difference-of-convex algorithm (DCA) [39, 48, 53]. Writing it as the difference of two convex models, and linearizing the convex one containing $\|\cdot\|_{2,1}$ term, one can solve it using the split Bregman [54] or primal-dual [55, 56, 57] technique. Here we consider a primal-dual splitting algorithm based on the predual form of TV.

Based on the predual form of the $\|\cdot\|_{2,1}$, the corresponding saddle-point problem can be written as

$$\min_u \frac{1}{2\lambda} \|W \odot (\mathcal{P}u - Y)\|^2 + \mathbb{I}_U(u) + \|\nabla u\|_1 - \alpha \max_{\|q\|_{2,\infty} \leq 1} -\langle \nabla u, q \rangle,$$

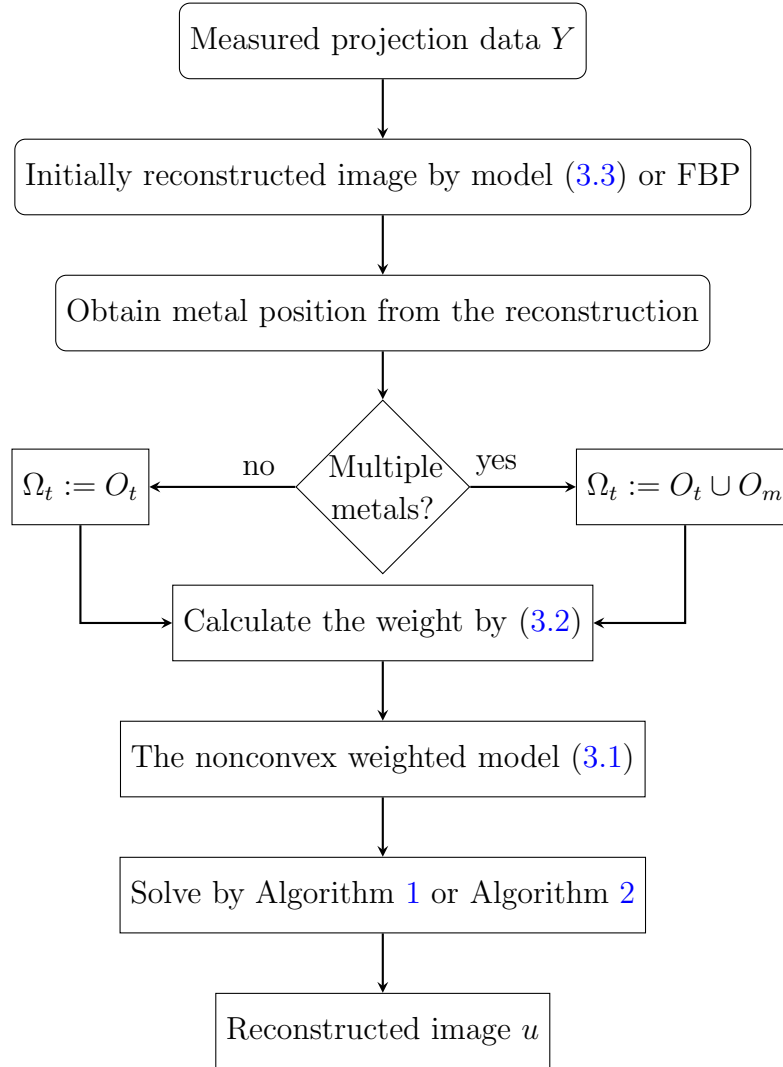


Figure 2: Flowchart of the proposed CT image reconstruction with reduced metal artifacts.

where $\mathbb{I}_U(u)$ is the indicator function regarding a closed set U :

$$\mathbb{I}_U(u) := \begin{cases} 0 & \text{if } u \in U, \\ +\infty & \text{otherwise} \end{cases}$$

with $U := \{u \in X : 0 \leq u_{i,j} \leq c \ \forall i, j\}$, $\|q\|_{2,\infty} := \max_{1 \leq i, j \leq n} \sqrt{\|(q_x)_{i,j}\|^2 + \|(q_y)_{i,j}\|^2}$ and $\langle \cdot, \cdot \rangle$ denotes the inner product. It can be rewritten equivalently as the following optimization problem

$$\min_{u, q} \frac{1}{2\lambda} \|W \odot (\mathcal{P}u - Y)\|^2 + \mathbb{I}_U(u) + \|\nabla u\|_1 + \alpha \langle \nabla u, q \rangle + \mathbb{I}_Q(q)$$

with $Q := \{q \in X \times X : \sqrt{(q_x)_{i,j}^2 + (q_y)_{i,j}^2} \leq 1 \ \forall i, j\}$. Further based on the predual

form of $\|\cdot\|_1$, it can be rewritten as

$$\min_{u,q} \max_p \frac{1}{2\lambda} \|W \odot (\mathcal{P}u - Y)\|^2 + \mathbb{I}_U(u) + \langle \nabla u, p + \alpha q \rangle - \mathbb{I}_S(p) + \mathbb{I}_Q(q), \quad (3.4)$$

where $S := \{p \in X \times X, |(p_x)_{i,j}| \leq 1, |(p_y)_{i,j}| \leq 1 \ \forall i, j\}$.

In order to guarantee the convergence of the splitting algorithm for such nonconvex optimization model, an additional quadratic term is added to (3.4), such that one immediately gets the penalized model below

$$\begin{aligned} \min_{u,q} \max_p \frac{1}{2\lambda} \|W \odot (\mathcal{P}u - Y)\|^2 + \mathbb{I}_U(u) + \langle \nabla u, p + \alpha q \rangle \\ - \mathbb{I}_S(p) + \mathbb{I}_Q(q) - \frac{\eta}{2} \|p\|^2. \end{aligned} \quad (3.5)$$

The above optimization problem w.r.t. the variable p is strongly concave. Note that it can return to the original model (3.4) only if $\eta = 0$. We remark that such penalization is to enhance the smoothness of the normalized gradient of the image.

Letting $G(u) := \frac{1}{2\lambda} \|W \odot (\mathcal{P}u - Y)\|^2 + \mathbb{I}_U(u)$, $f(\cdot) := \|\cdot\|_1$ and $g(\cdot) := \|\cdot\|_{2,1}$, $f_\eta^*(p) := f^*(p) + \frac{\eta}{2} \|p\|^2$ with f^* being itself the convex conjugate, the saddle point problem (3.5) is rewritten as follows

$$\min_{u,q} \max_p L_{PD}(u, q, p) \quad (3.6)$$

with

$$L_{PD}(u, q, p) := G(u) + \langle \nabla u, p + \alpha q \rangle - f_\eta^*(p) + g^*(q).$$

3.2.1 Preconditioned primal-dual hybrid gradient A natural scheme to solve the above saddle point problem is to split them, which consists of following preconditional version [58] of the u subproblem and three-step iterations for the generalized primal-dual hybrid gradient (PDHG):

$$\begin{cases} \text{Step 1:} & u^{k+1} = \arg \min_u L_{PD}(u, q^k, p^k) + \frac{\|u - u^k\|_{\mathcal{M}_\lambda}^2}{2}, \\ \text{Step 2:} & \bar{u}^{k+1} = 2u^{k+1} - u^k, \\ \text{Step 3:} & q^{k+1} = \arg \min_q L_{PD}(\bar{u}^{k+1}, q, p^k) + \frac{\|q - q^k\|^2}{2\tau}, \\ \text{Step 4:} & p^{k+1} = \arg \max_p L_{PD}(\bar{u}^{k+1}, q^{k+1}, p) - \frac{\|p - p^k\|^2}{2\beta}. \end{cases} \quad (3.7)$$

with positive definite operator $\mathcal{M}_\lambda : X \rightarrow X$ (we call it preconditioning operator and give the specific definition later), where $\|u\|_{\mathcal{M}_\lambda}^2 := \langle \mathcal{M}_\lambda u, u \rangle$. Here we remark that the operator \mathcal{M}_λ is selected such that not only the u -subproblem in Step 1 has a closed form solution, but also the convergence of the Algorithm 1 can be guaranteed. Besides, since each subproblem is strictly convex, the solutions to the minimization problems are unique and therefore use “=”.

In order to derive the expression for \mathcal{M}_λ , rewrite the subproblem in Step 1 of (3.7) as

$$u^{k+1} = \arg \min_{u \in U} \left\{ \frac{1}{2\lambda} \|W \odot (\mathcal{P}u - Y)\|^2 + \langle \nabla u, p^k + \alpha q^k \rangle + \frac{1}{2} \|u - u^k\|_{\mathcal{M}_\lambda}^2 \right\}.$$

Regardless of the constraint, the derivative of the subproblem is calculated as

$$\begin{aligned} & \frac{1}{\lambda} \mathcal{P}^T (W \odot W \odot (\mathcal{P}u - Y)) - \operatorname{div}(p^k + \alpha q^k) + \mathcal{M}_\lambda(u - u^k) \\ &= \left(\frac{1}{\lambda} \mathcal{P}^T (W \odot W \odot \mathcal{P}) + \mathcal{M}_\lambda \right) u - \frac{1}{\lambda} \mathcal{P}^T (W \odot W \odot Y) \\ & \quad - \operatorname{div}(p^k + \alpha q^k) - \mathcal{M}_\lambda u^k, \end{aligned}$$

where div is the divergence operator. Let \mathcal{M}_λ satisfies

$$\frac{1}{\lambda} \mathcal{P}^T (W \odot W \odot \mathcal{P}) + \mathcal{M}_\lambda = \gamma \mathcal{I} \quad (3.8)$$

with $\gamma > 0$ and \mathcal{I} being identity operator. Immediately for u -subproblem, one just needs to solve the following constrained quadratic problem

$$u^{k+1} = \arg \min_{u \in U} \left\{ \frac{1}{2} \left\| u - \frac{1}{\gamma} \left(\frac{1}{\lambda} \mathcal{P}^T (W \odot W \odot Y) + \operatorname{div}(p^k + \alpha q^k) + \mathcal{M}_\lambda u^k \right) \right\|^2 \right\}.$$

The close-form solution of Step 1 is given as

$$u^{k+1} = \frac{1}{\gamma} \operatorname{Proj} \left(\frac{1}{\lambda} \mathcal{P}^T (W \odot W \odot Y) + \operatorname{div}(p^k + \alpha q^k) + \mathcal{M}_\lambda u^k; U \right) \quad (3.9)$$

with the projection operator defined as

$$\operatorname{Proj}(u; U) := \min \{ \max \{u, 0\}, c \}.$$

Second, consider the subproblem in Step 3 of (3.7) w.r.t. the variable q as

$$q^{k+1} = \arg \min_{q \in Q} \left\{ \alpha \langle \nabla \bar{u}^{k+1}, q \rangle + \frac{1}{2\tau} \|q - q^k\|^2 \right\}.$$

Consequently the close-form solution of Step 3 is given as

$$q^{k+1} = \operatorname{Proj} \left(q^k - \tau \alpha \nabla \bar{u}^{k+1}; Q \right) \quad (3.10)$$

with the projection operator defined as

$$[\operatorname{Proj}(q; Q)]_{i,j} := \frac{q_{i,j}}{\max \left(1, \sqrt{(q_x)_{i,j}^2 + (q_y)_{i,j}^2} \right)}.$$

Finally, the subproblem w.r.t. the variable p reads

$$p^{k+1} = \operatorname{Proj} \left(\frac{1}{1 + \eta\beta} (p^k + \beta \nabla \bar{u}^{k+1}); S \right) \quad (3.11)$$

with the projection operator defined as

$$[\operatorname{Proj}(p; S)]_{i,j} := \frac{p_{i,j}}{\max \left(1, |(p_x)_{i,j}|, |(p_y)_{i,j}| \right)}.$$

Algorithm 1 Pre-PDHG for Model (3.6)

Input: Set $q^0 = 0$, $p^0 = 0$, parameters λ , α , η , γ , τ and β , maximum iteration number N , and tolerate accuracy tol .

Output: sample in the spatial domain.

- 1: **for** $k = 1 \rightarrow N$ **do**
- 2: **if** Stopping criteria is not met **then**
- 3: Compute u^{k+1} by (3.9).
- 4: Update \bar{u}^{k+1} as Step 2 of (3.7).
- 5: Compute q^{k+1} by (3.10).
- 6: Compute p^{k+1} by (3.11).
- 7: **return** u

Based on the above calculations, the preconditioned primal-dual hybrid gradient (Pre-PDHG) for Model (3.6) is summarized in Algorithm 1.

In Algorithm 1 the parameter γ has to be selected to be big enough in order to satisfy the setting of the precondition, resulting in slow convergence. It is necessary to seek an alternative splitting method with fast convergence.

3.2.2 Fully-splitting primal-dual hybrid gradient A natural idea is to introduce the constraint $v = \mathcal{P}u$ and add it to the objective function with the Lagrange multiplier $\Lambda \in \mathbb{R}^{m_1 \times m_2}$ as below

$$L(u, v, q, p, \Lambda) := \frac{1}{2\lambda} \|W \odot (v - Y)\|^2 + \mathbb{I}_U(u) + \langle \Lambda, v - \mathcal{P}u \rangle + \langle \nabla u, p + \alpha q \rangle - \mathbb{I}_S(p) + \mathbb{I}_Q(q) - \frac{\eta}{2} \|p\|^2. \quad (3.12)$$

Consequently, one needs to solve a saddle point problem as follows:

$$\min_{u, q, v} \max_{p, \Lambda} L(u, v, q, p, \Lambda).$$

The scheme of the fully-splitting PDHG (FS-PDHG) in the $(k+1)$ _{th} iteration can be described as:

$$\left\{ \begin{array}{l} \text{Step 1: } \Lambda^{k+1} = \Lambda^k + \rho(v^k - \mathcal{P}u^k), \\ \text{Step 2: } u^{k+1} = \arg \min_u L(u, v^k, q^k, p^k, \Lambda^{k+1}) + \frac{\|u - u^k\|^2}{2\sigma_1}, \\ \text{Step 3: } \bar{u}^{k+1} = 2u^{k+1} - u^k, \\ \text{Step 4: } v^{k+1} = \arg \min_v L(\bar{u}^{k+1}, v, q^k, p^k, \Lambda^{k+1}) + \frac{\|v - v^k\|^2}{2\sigma_2}, \\ \text{Step 5: } q^{k+1} = \arg \min_q L(\bar{u}^{k+1}, v^{k+1}, q, p^k, \Lambda^{k+1}) + \frac{\|q - q^k\|^2}{2\tau}, \\ \text{Step 6: } p^{k+1} = \arg \max_p L(\bar{u}^{k+1}, v^{k+1}, q^{k+1}, p, \Lambda^{k+1}) - \frac{\|p - p^k\|^2}{2\beta} \end{array} \right. \quad (3.13)$$

with positive parameters ρ , σ_1 , σ_2 , τ and β . Here we remark that these subproblems w.r.t. the variables u , v , q , and p are strictly convex and have closed form solutions.

First, we consider the subproblem w.r.t. the variable u :

$$u^{k+1} = \arg \min_{u \in U} \langle \nabla u, p^k + \alpha q^k \rangle + \langle \Lambda^{k+1}, -\mathcal{P}u \rangle + \frac{1}{2\sigma_1} \|u - u^k\|^2.$$

Similarly to (3.9), one readily obtains the solution:

$$u^{k+1} = \text{Proj}\left(\sigma_1 \text{div}(p^k + \alpha q^k) + \sigma_1 \mathcal{P}^T \Lambda^{k+1} + u^k; U\right). \quad (3.14)$$

Next, we consider the subproblem w.r.t. the variable v . The closed-form solution can be directly derived as follows:

$$v^{k+1} = \left(\frac{1}{\sigma_2} v^k - \Lambda^{k+1} + \frac{1}{\lambda} Y \odot W \odot W\right) / \left(\frac{1}{\sigma_2} + \frac{1}{\lambda} W \odot W\right). \quad (3.15)$$

Regarding the subproblems w.r.t. q and p , their solutions are directly given below following (3.10) and (3.11):

$$\begin{aligned} q^{k+1} &= \text{Proj}\left(q^k - \tau \alpha \nabla \bar{u}^{k+1}; Q\right), \\ p^{k+1} &= \text{Proj}\left(\frac{1}{1 + \eta \beta} (p^k + \beta \nabla \bar{u}^{k+1}); S\right). \end{aligned} \quad (3.16)$$

Finally, we summarize the FS-PDHG scheme in Algorithm 2.

Algorithm 2 FS-PDHG for Model (3.6)

Input: Set $u^0, v^0, q^0, p^0 = 0$, parameters $\lambda, \alpha, \eta, \rho, \sigma_1, \sigma_2, \tau$ and β , maximum iteration number N , and tolerate accuracy tol .

Output: sample in the spatial domain.

- 1: **for** $k = 1 \rightarrow N$ **do**
 - 2: **if** Stopping criteria is not met **then**
 - 3: Update the multiplier as Step 4 of (3.13).
 - 4: Compute u^{k+1} by (3.14).
 - 5: Update \bar{u}^{k+1} as Step 3 of (3.13).
 - 6: Compute v^{k+1} by (3.15).
 - 7: Compute q^{k+1}, p^{k+1} in parallel by (3.16).
 - 8: **return** u
-

4 Convergence analysis

First, we give the general framework [59, 53, 60] for the convergence analysis of non-convex optimization iterative algorithms. Assuming that $\Phi : \mathbb{R}^d \rightarrow (-\infty, +\infty]$ is proper and lower semicontinuous, we consider the following minimization problem:

$$\min_z \Phi(z).$$

The iterative sequence $\{z^k\}_{k=0}^\infty$ is generated by any general algorithm \mathcal{A} for solving the above problem. First recall the definition concerning subdifferential calculus.

Definition 1. (Subdifferentials [61]) Let $\Phi : \mathbb{R}^d \rightarrow (-\infty, +\infty]$ be a proper and lower semicontinuous function.

(1) For a given $x \in \text{dom}\Phi$, the Fréchet subdifferential of Φ at x , written as $\hat{\partial}\Phi(x)$, is the set of all vectors $u \in \mathbb{R}^d$ which satisfy

$$\liminf_{y \neq x, y \rightarrow x} \frac{\Phi(y) - \Phi(x) - \langle u, y - x \rangle}{\|y - x\|} \geq 0$$

with $\text{dom}\Phi := \{x \in \mathbb{R}^d : \Phi(x) < +\infty\}$, and the notations $\langle \cdot \rangle$ and $\|\cdot\|$ being defined as the standard inner product and ℓ_2 norm in vector space \mathbb{R}^d respectively. When $x \notin \text{dom}\Phi$, we set $\hat{\partial}\Phi(x) = \emptyset$.

(2) The limiting-subdifferential, or simply the subdifferential, of Φ at $x \in \mathbb{R}^d$, written as $\partial\Phi(x)$, is defined through the following closure process

$$\partial\Phi(x) := \left\{ u \in \mathbb{R}^d : \exists x^k \rightarrow x, \Phi(x^k) \rightarrow \Phi(x) \text{ and } u^k \in \hat{\partial}\Phi(x^k) \rightarrow u \text{ as } k \rightarrow \infty \right\}.$$

For a general non-convex optimization problem, the expectation is to prove that the whole sequence generated by the algorithm \mathcal{A} converges to a critical point of Φ . Generally speaking, the subsequence convergence of $\{z^k\}$ can be obtained easily applying the following analytical framework [59]. If Φ satisfies the KL property [59], the iterative sequence can be further proved to be a Cauchy sequence such that the global convergence can be reached. Specifically, the following three conditions are adopted to prove the convergence of the algorithm:

- Sufficient descent: \mathcal{A} is essentially a descent algorithm, and each step has one lower bound estimation:

$$\Phi(z^k) - \Phi(z^{k+1}) \geq \rho_1 \|z^{k+1} - z^k\|^2 \quad k = 0, 1, \dots \quad (4.1)$$

with a positive constant ρ_1 .

- Upper bound of the subgradient:

$$\|\omega^{k+1}\| \leq \rho_2 \|z^{k+1} - z^k\|, \omega^{k+1} \in \partial\Phi(z^{k+1}) \quad k = 0, 1, \dots \quad (4.2)$$

with a positive constant ρ_2 .

- Kurdyka–Lojasiewicz (KL) property [59].

Next, we prove the convergence of the proposed algorithms step by step in the following parts. The successive errors of the iterative sequence are defined as:

$$\begin{aligned} E_u^{k+1} &:= u^{k+1} - u^k, E_q^{k+1} := q^{k+1} - q^k, E_p^{k+1} := p^{k+1} - p^k, \\ E_v^{k+1} &:= v^{k+1} - v^k, E_\Lambda^{k+1} := \Lambda^{k+1} - \Lambda^k. \end{aligned}$$

4.1 Convergence of Algorithm 1

The following analysis relies heavily on the auxiliary sequence defined below

$$L_\lambda(u, q, p, \tilde{u}) := G(u) + g^*(q) - f_\eta^*(p) + \langle \nabla u, p + \alpha q \rangle + \frac{1}{2} \|u - \tilde{u}\|_{\mathcal{M}_\lambda}^2. \quad (4.3)$$

The first-order optimality conditions for subproblems of (3.7) are given as follows

$$\operatorname{div}(p^k + \alpha q^k) + \mathcal{M}_\lambda(u^k - u^{k+1}) \in \partial G(u^{k+1}), \quad (4.4)$$

$$-\alpha \nabla \bar{u}^{k+1} + \frac{q^k - q^{k+1}}{\tau} \in \partial g^*(q^{k+1}), \quad (4.5)$$

$$\nabla \bar{u}^{k+1} + \frac{p^k - p^{k+1}}{\beta} \in \partial f_\eta^*(p^{k+1}). \quad (4.6)$$

Condition 1. *The three positive parameters τ, α, η satisfy*

$$2 - K\tau\alpha > 0, \quad \mathcal{M}_\lambda - \left(\frac{2K^2}{\eta} + K\alpha \right) \mathcal{I} \succ 0,$$

with $\cdot \succ 0$ denoting strictly positive definite and K being a bound on the norm of the linear operator ∇ .

Using formula (4.4), G , g^* convexity and the k _{th} update of p , the following Proposition 4.1 can be derived readily.

Proposition 4.1. *For all $k \geq 0$, we have*

$$G(u^k) - G(u^{k+1}) \geq \langle \nabla(u^{k+1} - u^k), p^k + \alpha q^k \rangle + \|E_u^{k+1}\|_{\mathcal{M}_\lambda}^2, \quad (4.7)$$

$$g^*(q^k) - g^*(q^{k+1}) \geq \langle \alpha \nabla \bar{u}^{k+1}, q^{k+1} - q^k \rangle + \frac{1}{\tau} \|E_q^{k+1}\|^2, \quad (4.8)$$

$$\begin{aligned} f_\eta^*(p^{k+1}) - f_\eta^*(p^k) &\geq \langle \nabla \bar{u}^k, p^{k+1} - p^k \rangle + \left(\frac{\eta}{2} + \frac{1}{2\beta} \right) \|E_p^{k+1}\|^2 \\ &\quad + \frac{\|E_p^k\|^2}{2\beta} - \frac{\|p^{k+1} - p^{k-1}\|^2}{2\beta}. \end{aligned} \quad (4.9)$$

Lemma 4.1. *If $X^* := (u^*, q^*, p^*, \tilde{u}^*)$ is a critical point of the function L_λ , then (u^*, q^*, p^*) is a critical point of L_{PD} . Meanwhile, when $\eta = 0$, u^* is a critical point of the original model (3.1).*

The corresponding proof can be found in Appendix A.

Letting $X^k := (u^k, q^k, p^k, u^{k-1})$ be generated by Algorithm 1, we first estimate a sufficient descent of L_λ as shown in (4.1).

Lemma 4.2. *For all $k > 0$, under Condition 1, we obtain*

$$L_\lambda(X^k) - L_\lambda(X^{k+1}) \geq C \|X^{k+1} - X^k\|^2,$$

where $C := \min \left\{ C_1, \frac{1}{\tau} - \frac{K\alpha}{2}, \frac{\eta}{2} - K\xi_1 \right\}$ with C_1 being the minimum eigenvalue of the operator $\mathcal{M}_\lambda - \left(\frac{2K^2}{\eta} + K\alpha \right) \mathcal{I}$.

The corresponding proof can be found in Appendix B. The following Lemma represents the boundedness of $\{X^k\}$ and $\{L_\lambda(X^k)\}$.

Lemma 4.3. *The sequence $\{X^k\}$ generated by Algorithm 1 is bounded. Furthermore, the auxiliary sequence $\{L_\lambda(X^k)\}$ is bounded and nonincreasing.*

The proof can be found in Appendix C. To prove that the sequence approaches a critical point, similar to (4.2), we need the following results.

Lemma 4.4. *For all $k \geq 0$, we get*

$$\text{dist}(0, \partial L_\lambda(X^{k+1})) \leq C_2 \|X^{k+1} - X^k\| \quad (4.10)$$

with a positive constant $C_2 := 2 \max \{K + K\alpha + \|\mathcal{M}_\lambda\|, \frac{1}{\tau} + K\alpha, \frac{1}{\beta} + K\}$.

The corresponding proof can be found in Appendix D.

Our objective is to prove the convergence of the entire sequence generated by Algorithm 1 to a critical point of (4.3). To accomplish this, we discuss whether the optimization function satisfies the KL property. It is trivial to see that $G(u) + \langle \nabla u, p + \alpha q \rangle + \frac{1}{2} \|u - \tilde{u}\|_{\mathcal{M}_\lambda}^2 - \frac{\eta}{2} \|p\|^2$ is the semi-algebraic function as well as the indicator functions $g^*(q) - f^*(p)$, such that L_λ is semi-algebraic [62], which satisfies the KL property.

Theorem 4.1. *Under Condition 1, the iterative sequence $\{X^k\}$ generated by Algorithm 1 converges to a critical point X^* of L_λ .*

The proof of Theorem 4.1 follows standard techniques [59, 53, 60] and is therefore omitted here.

4.2 Convergence of Algorithm 2.

Similar to (4.3), according to the iteration scheme (3.13), the auxiliary sequence is given as follows

$$\begin{aligned} L_\sigma(\Lambda, u, v, q, p, \tilde{u}, \tilde{v}) := & F(v) + h(u) + g^*(q) - f_\eta^*(p) + \langle \nabla u, p + \alpha q \rangle \\ & + \langle \Lambda, v - \mathcal{P}u \rangle + \frac{1}{2\sigma_1} \|u - \tilde{u}\|^2 + \frac{1}{2\sigma_2} \|v - \tilde{v}\|^2 \end{aligned} \quad (4.11)$$

with $F(v) := \frac{1}{2\lambda} \|W \odot (v - Y)\|^2$ and $h(u) := \mathbb{I}_U(u)$.

Condition 2. *The parameters $\lambda, \tau, \alpha, \sigma_1, \sigma_2, \eta$ and ρ satisfy*

$$2 - K\tau\alpha > 0, \quad \frac{K\sigma_1}{1 - K\alpha} < \frac{\eta}{2K}, \quad \frac{1}{2\sigma_2} - \frac{4}{\rho} \left(\frac{1}{\lambda^2} \|W\|_{\max}^4 + \frac{1}{\sigma_2^2} \right) > 0.$$

Lemma 4.5. *Let $Z^* := (\Lambda^*, u^*, v^*, q^*, p^*, \tilde{u}^*, \tilde{v}^*)$ be a critical point of the functional L_σ . Then $(u^*, v^*, q^*, p^*, \Lambda^*)$ is a critical point of L . Moreover, when $\eta = 0$, u^* is a critical point of the original model (3.1).*

The corresponding proof can be found in Appendix E.

Denoting $Z^k := (\Lambda^k, u^k, v^k, q^k, p^k, u^{k-1}, v^{k-1})$, the following relations hold as follows.

Lemma 4.6. *For all $k > 0$, we have*

$$L_\sigma(Z^k) - L_\sigma(Z^{k+1}) \geq \tilde{C} \|Z^{k+1} - Z^k\|^2,$$

where

$$\tilde{C} := \min \left\{ \frac{1}{2\sigma_1} - \frac{K}{2\xi_2}, \frac{\eta}{2} - \frac{K}{\xi_2}, \frac{1}{2\sigma_1} - \frac{K}{2\xi_2} - \frac{K\alpha}{2}, \frac{1}{2\sigma_2} - \frac{4}{\rho} \left(\frac{1}{\lambda^2} \|W\|_{\max}^4 + \frac{1}{\sigma_2^2} \right) \right\}.$$

The corresponding proof can be found in Appendix F.

The introduction of the Lagrange multiplier results in L_σ being non-coercive, which precludes easily proving the boundedness of $\{Z^k\}$. Thus, we hereby assume the boundedness of $\{v^k\}$.

Assumption 1. *The sequence $\{v^k\}$ generated by Algorithm 2 is bounded.*

Lemma 4.7. *Under Assumption 1, the sequence $\{Z^k\}$ generated by Algorithm 2 is bounded. Furthermore, the auxiliary sequence $\{L_\sigma(Z^k)\}$ is bounded and nonincreasing.*

The proof follows directly in a similar manner to that of Lemma 4.3. Additionally, the following results are needed.

Lemma 4.8. *For all $k \geq 0$, we obtain*

$$\text{dist}(0, \partial L_\sigma(Z^{k+1})) \leq C_3 \|Z^{k+1} - Z^k\| + \frac{1}{\rho} \|Z^{k+2} - Z^{k+1}\| \quad (4.12)$$

with a positive constant $C_3 := 2 \max \left\{ K + K\alpha + \frac{1}{\sigma_1}, \frac{1}{\tau} + K\alpha, \frac{1}{\beta} + K, \frac{1}{\sigma_2} \right\}$.

The proof follows in a similar manner to Lemma 4.4 and thus we omit it here. Ultimately, the aforementioned results allow us to establish the final convergence theorem.

Theorem 4.2. *Under Assumption 1 and Condition 2, the sequence $\{Z^k\}$ generated by Algorithm 2 converges to a critical point Z^* of L_σ , provided $1 - \frac{1}{\rho C_3} > 0$.*

5 Numerical experiments

In this section, we validate the accuracy of our model through simulation data in the first four sections and proceed to test its performance employing real data in the fifth section. All numerical experiments are implemented in MATLAB R2021a on a laptop with 4-cores 3.1 GHz Intel Core and 16 GB RAM.

5.1 Experimental settings

We utilize the fan-beam CT imaging system for all simulations. The distance from the source to the detector is 949.075 mm, the source to iso-center distance is 541 mm, and the strip width is 1.024 mm. A complete 360° rotation in a circular orbit comprises a total of 984 projected views, with each view containing 888 bins.

All the phantoms are composed of soft tissue, bone, and two circular metal objects. The specific linear attenuation coefficients for these objects can be found in reference [63]. Each reconstructed image comprises 256×256 pixels. In the NCAT phantom image (depicted in Figure 12(a)), the metal components are fabricated from titanium, whereas the iron is used for the other two phantoms (displayed in Figures 14(a) and 15(a)).

The simulated Y with the energy spectrum $\mathcal{S}_0(E)$ (as shown in Figure 3) is obtained from the projected data contaminated by Poisson noise in the following way [64]

$$Y_{i,j} = -\log\left(\max\{\text{Poisrnd}(S_0 e^{-Y_0(i,j)})/S_0, 1/S_0\}\right) \quad \forall i, j, \quad (5.1)$$

where $\text{Poisrnd}(\cdot)$ refers to the Poisson noise, S_0 is the number of incident photons, and the term $1/S_0$ is to avoid taking the logarithm of 0. We select $S_0 = 10^5$ for the NCAT phantom and $S_0 = 10^9$ for the other two in (5.1).

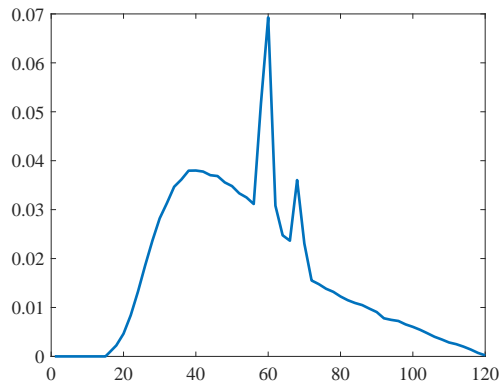


Figure 3: Energy spectrum $\mathcal{S}_0(E)$

The stopping criterion is defined as follows

$$\frac{\|u^{k+1} - u^k\|}{\|u^{k+1}\|} \leq tol.$$

For NCAT and head phantoms, we choose $tol = 9 \times 10^{-5}$, while for the skull, set it to 5×10^{-5} . For the weighted function W , the default values are set to $t = 0.94$ and $\varepsilon = 10^{-16}$.

5.2 Tests on various weight functions

We use the following two phantoms in Figure 4 to demonstrate the efficiency of the proposed weight function W . For a fair comparison, we change the regularization of the model (2.3) to the AITV:

$$u^* = \arg \min_u \frac{1}{2\lambda} \|B_\Omega^c \odot (\mathcal{P}u - Y)\|^2 + \|\nabla u\|_1 - \alpha \|\nabla u\|_{2,1}. \quad (5.2)$$

The results show that model (5.2) is relatively worse than the proposed model in balancing the reduction of metal artifacts and the sharpness of the image. In Figures 4(b)-4(c), the image reconstructed by the model (5.2) has severe diffusion near the metal (see the red arrow below), and almost the metal information is lost because there is no prior related to the metal. On the contrary, the proposed model performs significantly better near the bone. To provide a more detailed representation, we display the CT values of the two cutlines adjacent to the metal in Figure 5. The results shown in Figure 5(e) clearly demonstrate that the proposed model performs better in terms of correcting metal artifacts compared to model (5.2), as it exhibits a closer proximity

to the reference value. In particular, Figure 5(f) further highlights the superiority of our method, as it not only demonstrates a closer resemblance to the reference, but also exhibits favorable contrast (near pixel 185 in Figure 5(f)).

In the above test, O_m and O_t are almost the same. We will show an example with the large bone, leading to quite different regions (as shown in Figure 6). The results are put to Figures 4(d)-4(f), by considering the head phantom. Similarly, from Figure 4(d), one can see clear artifacts and boundary diffusion simply with the weight function in (5.2) (see red arrows). In Figure 4(e) obtained by replacing Ω_t with O_m in the weight function W of the proposed model, one readily sees that it is difficult to remove artifacts between metal and bone (see the blue arrow), while using the proposed weight function based on O_t and O_m , the metal artifacts are greatly reduced as shown in Figure 4(f).

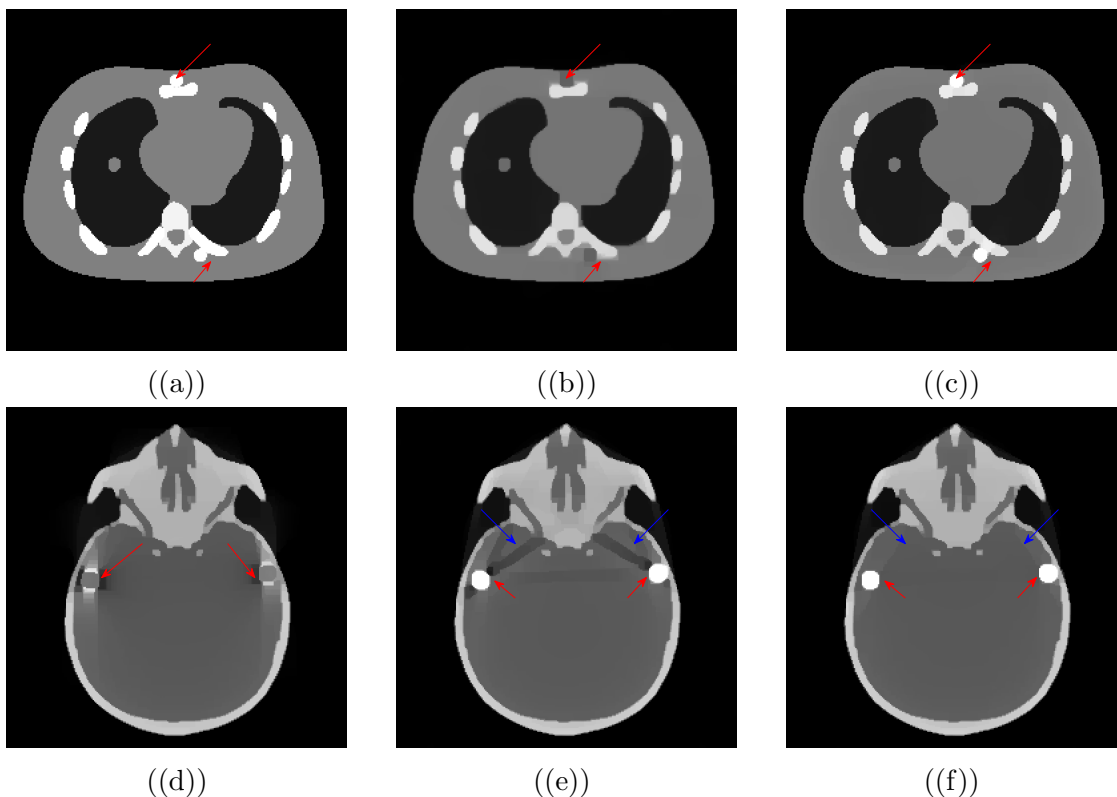


Figure 4: Comparison of the different weights. The first row is the reference image and the result of NCAT phantom in models (5.2) and (3.5), respectively (4600 HU window, 1300 HU level). The second row is the reconstruction result of the head phantom in model (5.2) and the selection of O_m or Ω_t as the mask region in (3.5) from left to right (4200 HU window, 1100 HU level).

5.3 Convergence validation and parameter impact

Convergence validation In order to numerically illustrate the convergence behavior of Algorithm 1 and Algorithm 2, the convergence curves of $\log_{10}\left(\frac{\|u^{k+1}-u^k\|}{\|u^{k+1}\|}\right)$ and the

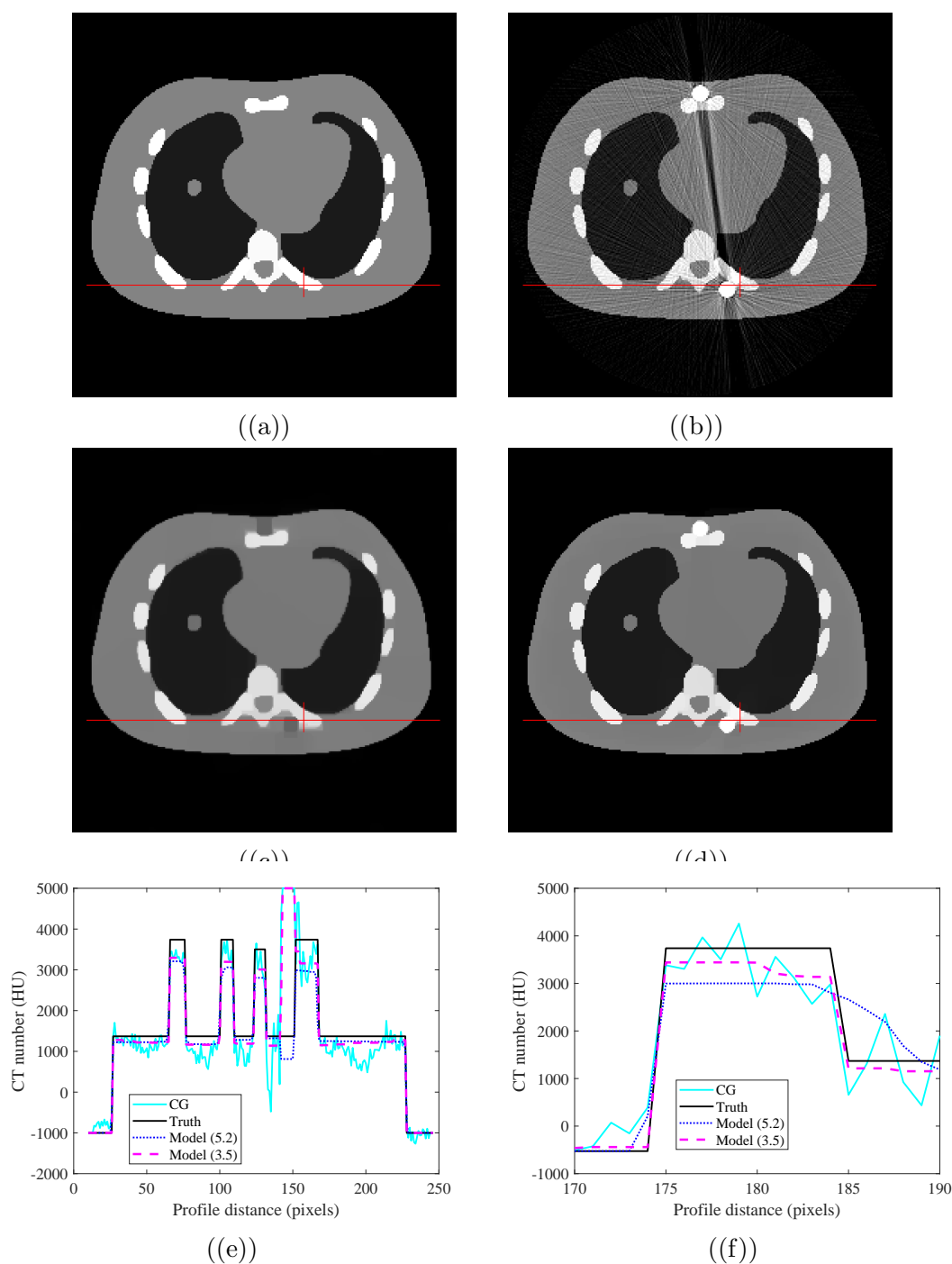


Figure 5: The third row represents the variation curve of Hounsfield Units (HU) corresponding to the positions of the red lines in the reconstructed images (5(a))-(5(d)). From left to right, it shows the horizontal profile and the vertical profile. The remaining two rows correspond to the real metal-free image, the CG reconstruction image, the reconstruction result of model (5.2), and the reconstruction result of model (3.5) (4600 HU window, 1300 HU level).

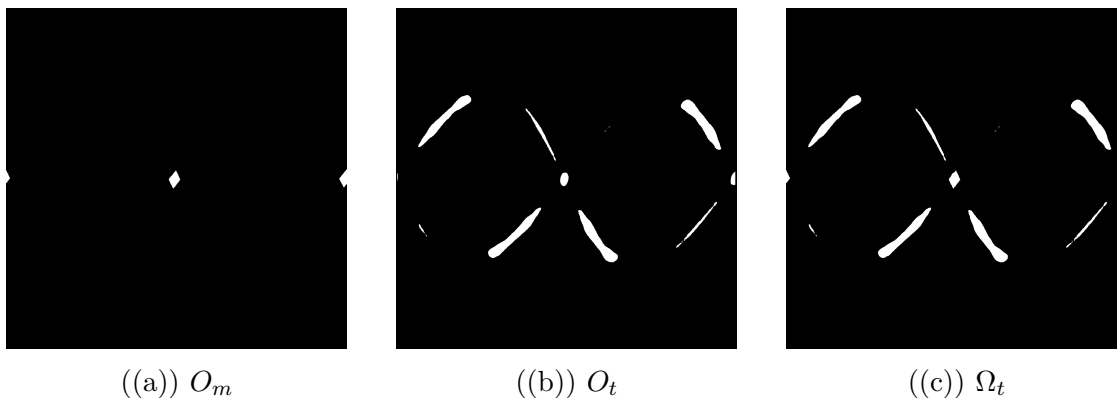


Figure 6: The mask region of the proposed weight for the head phantom. From left to right are O_m , O_t and Ω_t , respectively.

energy function is shown in Figure 7. One readily sees that though local oscillations appear for the proposed FS-PDHG algorithm, both the relative error and the energy keep decreasing during iterations, which is consistent with the convergence analysis in section 4. Moreover, it is evident that the FS-PDHG algorithm exhibits faster convergence compared to the Pre-PDHG algorithm since the former reaches the desired tolerance with much fewer iterations than the latter.

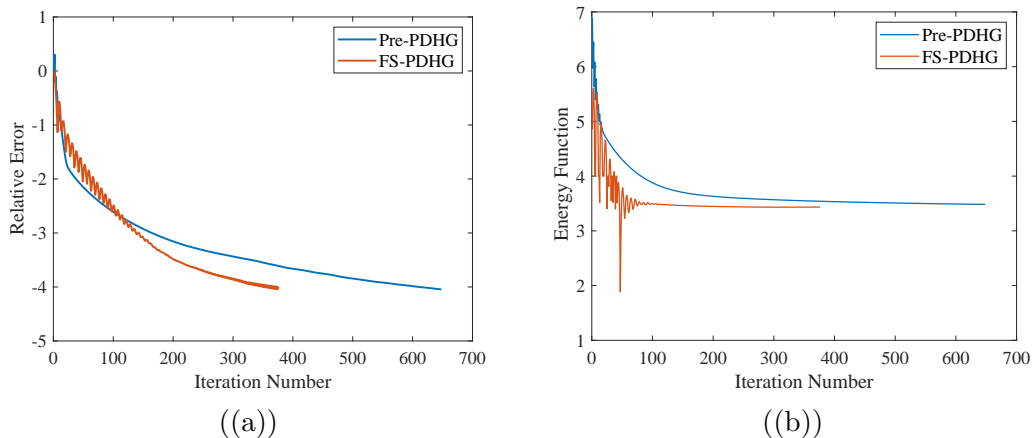


Figure 7: Convergence of Algorithm 1 and Algorithm 2 on the NCAT. From left to right are the curves for the relative error and energy function of the proposed algorithms, respectively.

Parameter impact We first test the performance of the proposed algorithms with different nonconvex regularization parameter α based on the NCAT. Table 1 records the reconstruction errors (normalized L^2 norm between the recovery result and the truth), SSIM and PSNR values with respect to the different values of α , where one readily sees that the proposed algorithms with proper parameter $\alpha = 0.75$ produce best results in terms of these three metrics, and the nonconvex regularization obtain the PSNR improvement of 1.5dB compared with the convex model by setting $\alpha = 0$. We

Table 1: Reconstruction error, SSIM and PSNR index of the NCAT phantom reconstructed by different α , i.e. $\alpha = 0, 0.25, 0.5, 0.75$ and 1 respectively.

α	Reconstruction error	SSIM	PSNR
0	0.1314	0.9766	28.1629
0.25	0.1103	0.9850	28.8709
0.5	0.1035	0.9883	29.4360
0.75	0.1003	0.9892	29.7163
1	0.1006	0.9891	29.6967

also put the visual results in Figure 8. One can see obvious diffusion near the metal when $\alpha = 0$. However, if $\alpha > 0$, particularly between the metal and bone, there is an improved boundary recovery, as depicted by the red circle in Figure 8(b). The blur effect is noticeably reduced at $\alpha \neq 0$. Among the different cases, $\alpha = 0.25$ exhibits relatively weaker improvement, as shown in the circled area below Figure 8(c). Comparing the results of $\alpha = 0.5$ with $\alpha = 0.75$, the recovered edges of the latter are sharper. The reconstructed images of $\alpha = 0.75$ and $\alpha = 1$ are very close, but the former yields better quantitative values according to Table 1. In order to further highlight the details, we display the contours (see Figure 10) framed in blue within the region where the metals are removed. The results within the red rectangle further demonstrate the effectiveness of such nonconvex regularization. Based on the experimental tests in Table 1 and Figure 8, we set $\alpha = 0.75$ as the default, unless otherwise specified. Figures 9(a)-9(b) demonstrate the disparity between the reference image and the outcomes obtained with $\alpha = 0$ and $\alpha = 0.75$, respectively. It is apparent that the boundary of the reconstruction with $\alpha = 0$ is not accurately depicted, whereas the results obtained with $\alpha = 0.75$ significantly enhance the boundary. By examining the absolute HU value curve (shown in Figures 9(c)-9(d)) along the red line in Figures 9(a)-9(b), the smaller the differences obtained with $\alpha = 0.75$, the better the reconstruction results. In contrast, the results obtained with $\alpha = 0$ exhibit noticeable jumps near the boundary, further indicating inaccurate boundary.

Next, we test the impact of other parameters for the proposed algorithms. To show how the algorithms vary w.r.t the parameters, we change the parameters in the following manner $c_0 \times 2^{k_0+r_0 \cdot l}$, where c_0 , k_0 and r_0 are constants dependent on the parameters of interest, and l represents the change frequency. Unless otherwise specified, the default values for k_0 and r_0 are both set to 1.

Experimental tests in Figures 11(a) and 11(d) show that η with $c_0 = 5 \times 10^{-6}$ is relatively insensitive when it is small, but the results demonstrate a threshold effect, whereby performance declines beyond a determinable upper bound. Besides, choose a proper $\eta = 10^{-4}$ as defaulted hereafter. Now let us consider the algorithm parameters, which include γ , τ and β . For the proposed Pre-PDHG, firstly, it can be observed by (3.8) that γ is highly dependent on λ and \mathcal{P} , thus we do not provide a specific

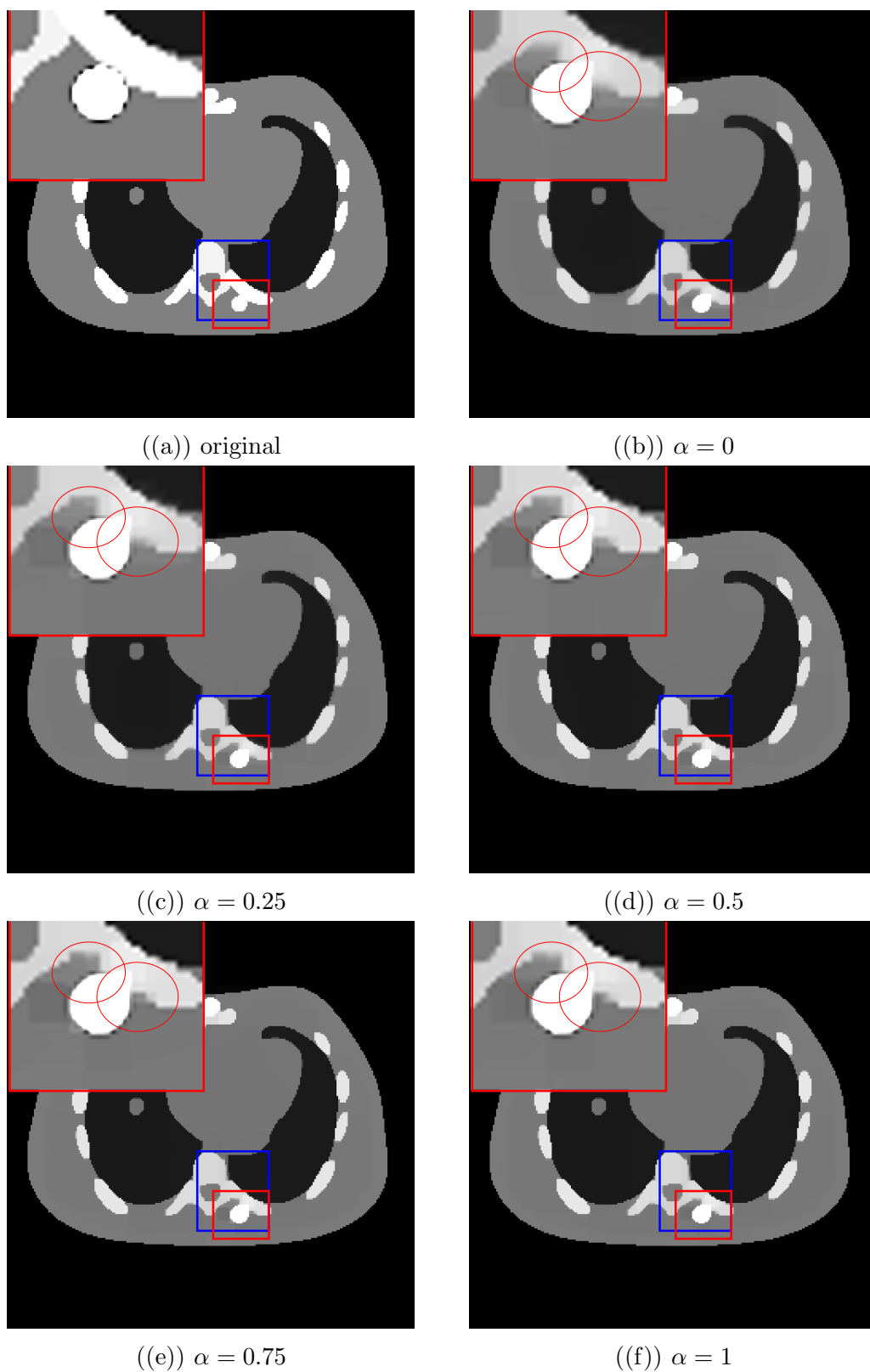


Figure 8: Comparison results with different parameters α (4600 HU window, 1300 HU level).

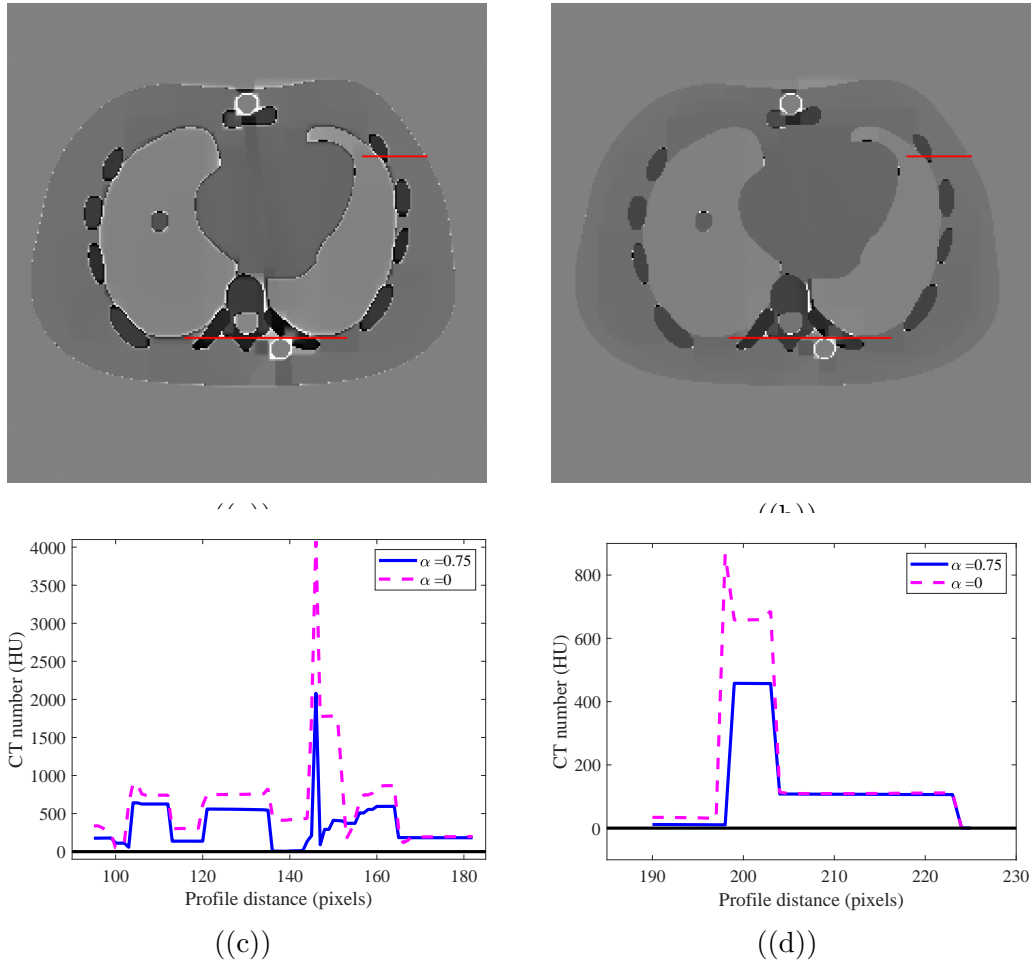


Figure 9: The first row represents the difference between the reconstruction results with parameters $\alpha = 0$ and $\alpha = 0.75$ and the reference image, and the second row displays the CT value curve highlighting the absolute value of the difference along the marked red line from left to right (2000 HU window, 0 HU level).

range. For τ and β with $k_0 = -5, c_0 = 5 \times 10^{-3}$, as depicted in Figures 11(b), 11(e), 11(c) and 11(f), the values do not exhibit significant variation with respect to these two parameters, empirically remaining within the approximate ranges of 0.01 and 5, respectively. Similarly, the parameter results for τ and β using the FS-PDHG algorithm exhibit comparable trends to those previously described. However, excessively small β values may induce oscillations. Therefore, we adjust its range to center around 50, setting the default $k_0 = 1$, while maintaining the same empirically-derived τ . For the remaining FS-PDHG parameters, we uniformly set r_0 to 0.25. The parameter ρ , with associated constants $c_0 = 1.2 \times 10^{-5}$ and $k_0 = 5.5$. Analysis indicates that excessively small ρ results in slow convergence, while excessively large ρ induces oscillations and failure to converge, as depicted in Figure 11(g). Based on the analysis, the recommended viable range for ρ is $[0.001, 0.01]$, with a default value of 0.003. Utilizing the same settings as ρ , we conduct an exploration of the effects induced by varying σ_1 , as depicted

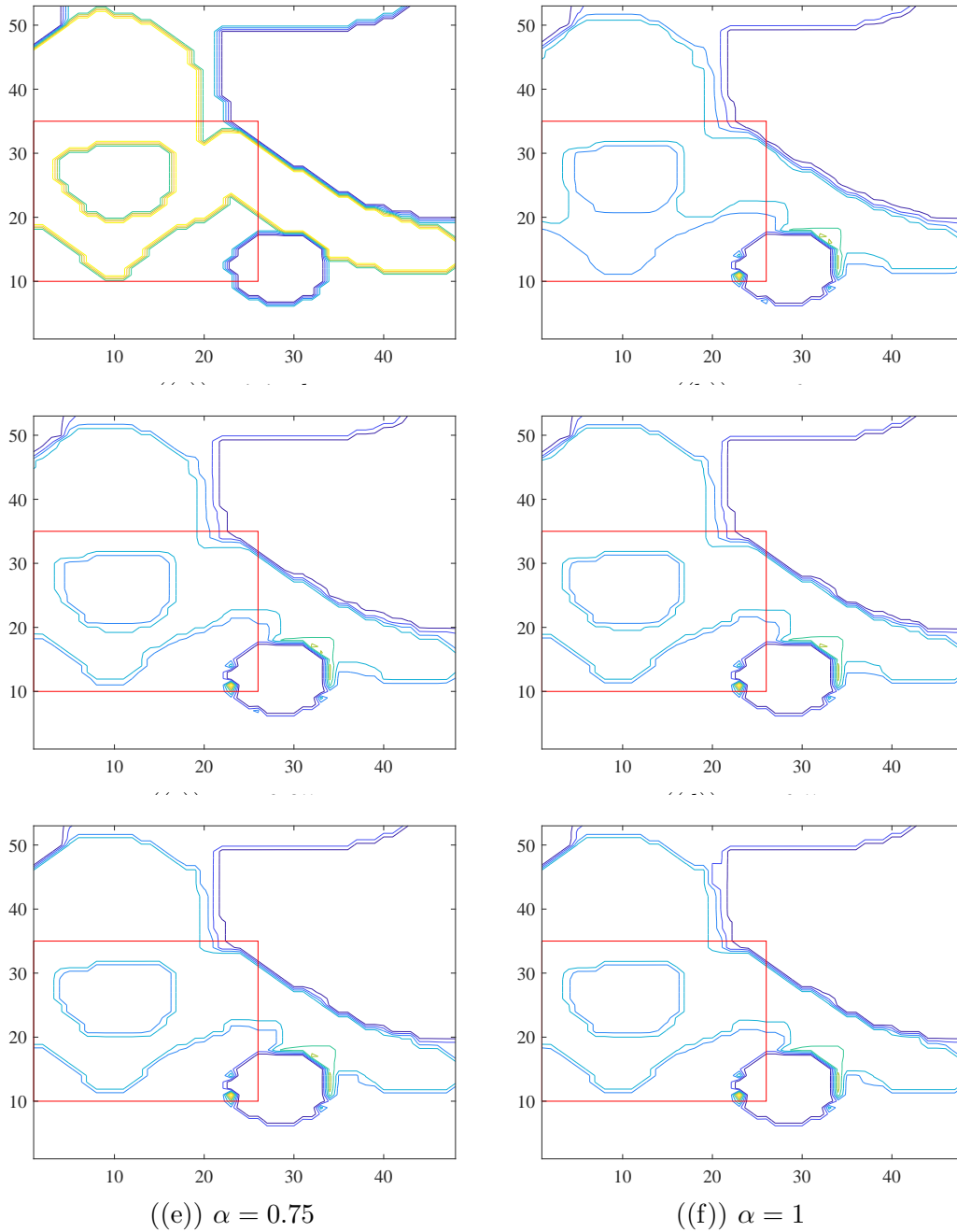


Figure 10: Comparison of contours with different parameters α .

in Figure 11(h). The results demonstrate that σ_1 exhibits relatively low sensitivity within a certain range. However excessive magnitudes lead to convergence failure. Empirically, we select σ_1 in the range of $[0.001, 0.01]$. Regarding σ_2 (see figure 11(i)), the associated constants are defined as $c_0 = 10^{-1}$ and $k_0 = 10$, respectively. Estimation reveals an optimal σ_2 centered around 300.

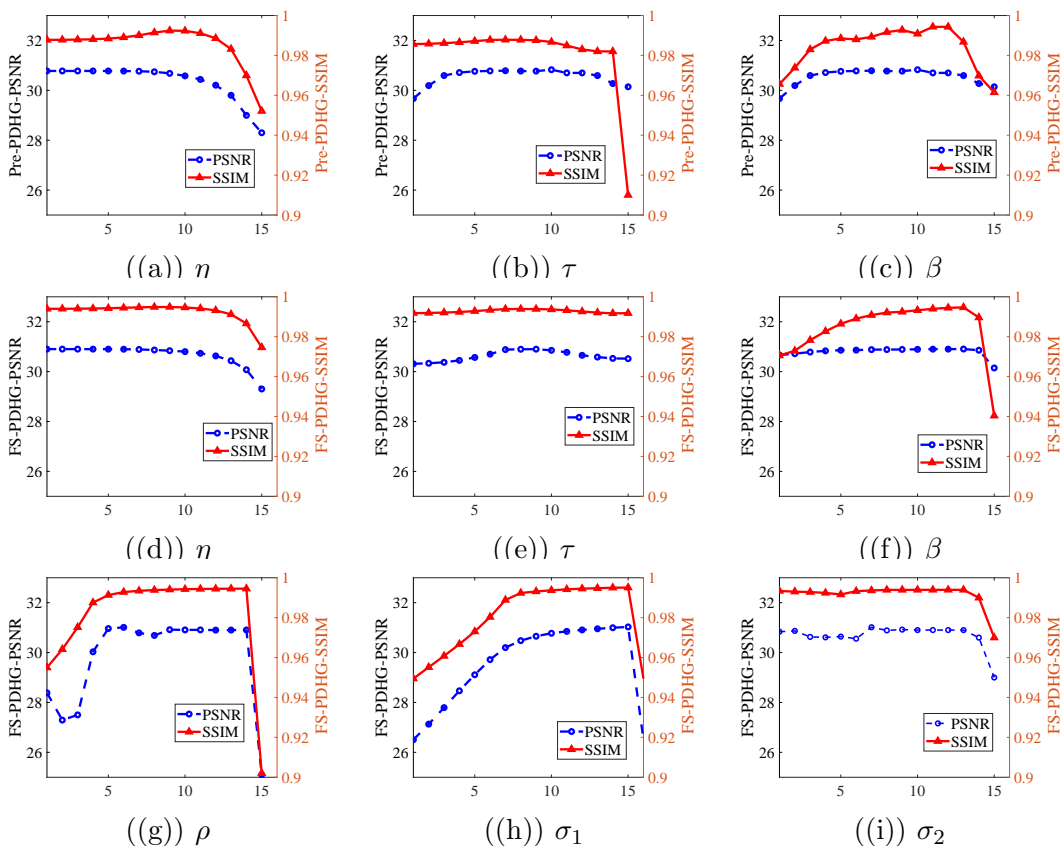


Figure 11: Parameter optimization results for the NCAT phantom. The first row depicts the PSNR and SSIM values obtained under varying η , τ , and β utilizing the Pre-PDHG algorithm. The second and third rows (Figures (d)-(i)) illustrate the performance of the FS-PDHG algorithm under adjustments to the parameters η , τ , β , ρ , σ_1 , and σ_2 , respectively.

5.4 Reconstructed results and comparisons

In this subsection, we further show the results by the proposed algorithms and compare them with those by CG, BCMAR [3], NMAR [13], TV-MAR (2.3) (solving by [57]), TV-TV inpainting [44], and Reweighted JSR [36]. The code of Reweighted JSR is provided by the authors of [36], while the remaining codes have been developed by ourselves. Results and comparisons between the proposed model and the above methods are shown in Figures 12, 14 and 15, respectively.

Figure 12(b) illustrates that the NCAT phantom reconstructed via the CG approach contains substantial metal artifacts and noise. As shown in Figure 12(c), the BCMAR corrector [3] fails to adequately address artifacts when high noise levels are present. While the NMAR approach (Figure 12(d)) admirably suppresses metal artifacts, blurriness around the metal regions exceeds that of TV-MAR. As depicted in Figure 12(e), the TV-MAR reconstructed result manifests negligible metal artifacts and noise. However, the metal components exhibit fusion with adjoining structures. The TV-

TV inpainting method yields improved results by reducing the excessive smoothing. However, there is still some diffusion present in the final output. The reconstructed images obtained utilizing Reweighted JSR model and the proposed model not only display negligible artifacts, but also remarkably preserve salient details. In Figure 13, we present the sinograms of the reconstructed results 12(i). Particularly in the magnified region, it is apparent that the proposed algorithm successfully suppresses the noise on the metal and bone traces depicted in Figure 13(c).

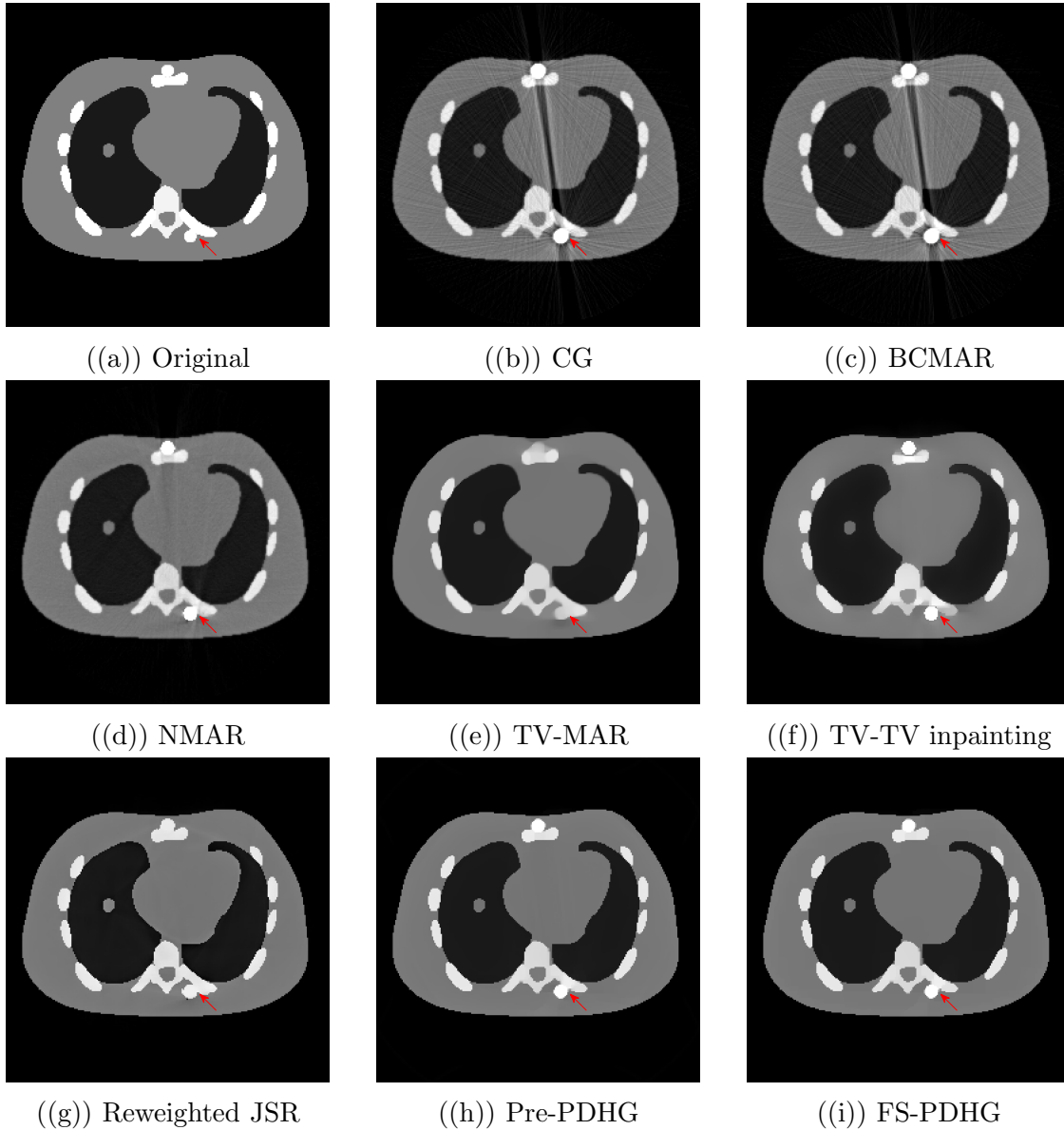


Figure 12: Comparison of reconstructed NCAT phantom. (a) Phantom image, (b) CG-reconstruction of the measured projection, (c)-(i) corrected images utilizing BCMAR, NMAR, TV-MAR, TV-TV inpainting, Reweighted JSR, Pre-PDHG and FS-PDHG, respectively (4600 HU window, 1300 HU level).

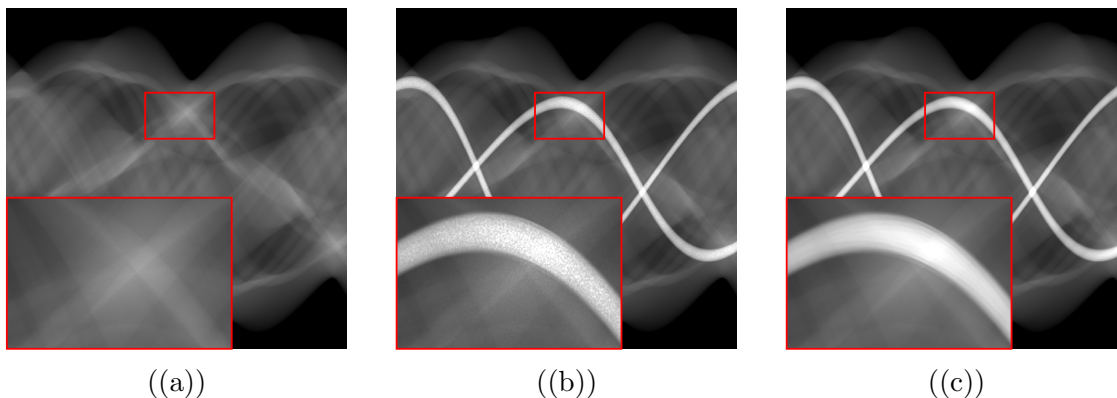


Figure 13: (a) Reference sinogram. (b) Measured sinogram. (c) The sinogram result from FS-PDHG.

Figure 14 displays the reconstructed images of the head phantom. This particular phantom poses greater challenges relative to the NCAT phantom, as it contains additional bone structures, yielding more prolific artifacts between the metals and bones alongside metal artifacts. The prior methods exhibit analogous consequences as the preceding examples. However, as observed in Figure 14(d), the outcomes of NMAR do not effectively recover regions near the bone, with artifacts still existing around the metals. Compared to the NCAT phantom, the enhanced artifacts arising between metals and bones detrimentally impact segmentation accuracy, engendering undesired structures in Figure 14(g) (structures around the red arrow) by Reweighted JSR. Nevertheless, akin to the NCAT phantom, the proposed method aptly corrects the metal artifacts as shown in Figures 14(h)-14(i).

Figure 15 exhibits the reconstructed skull phantom with more textures using various models. The result reconstructed by TV-MAR (Figure 15(e)) emerges significant artifacts. The inaccurate pre-segmentation result leads to the correction of metal artifacts by Reweighted JSR (Figure 15(g)) being insufficiently accurate. Analogous to prior phantom examples, the proposed algorithms persistently exhibit optimal comprehensive performance. Furthermore, Figure 16 illustrates the CT value distribution of the region of interest, providing further evidence that the results by our proposed method are more faithful to the ground truth.

The quantitative assessments of reconstructed image quality, encompassing reconstruction error, SSIM, PSNR values, and computation time, are delineated in Table 2. One readily discerns the enhancement conferred by Reweighted JSR and the proposed algorithms in terms of PSNR and SSIM, as compared to TV-MAR. In comparison to Reweighted JSR, the proposed algorithms (Pre-PDHG and FS-PDHG) can reconstruct competitive outcomes in terms of PSNR and SSIM, given accurate pre-segmentation (as in the case of NCAT). For less precise pre-segmentation, they can reconstruct significantly superior results, garnering PSNR escalations of 0.8dB and 1.8dB for the head and skull cases, respectively. Moreover, in comparison to Reweighted JSR, our

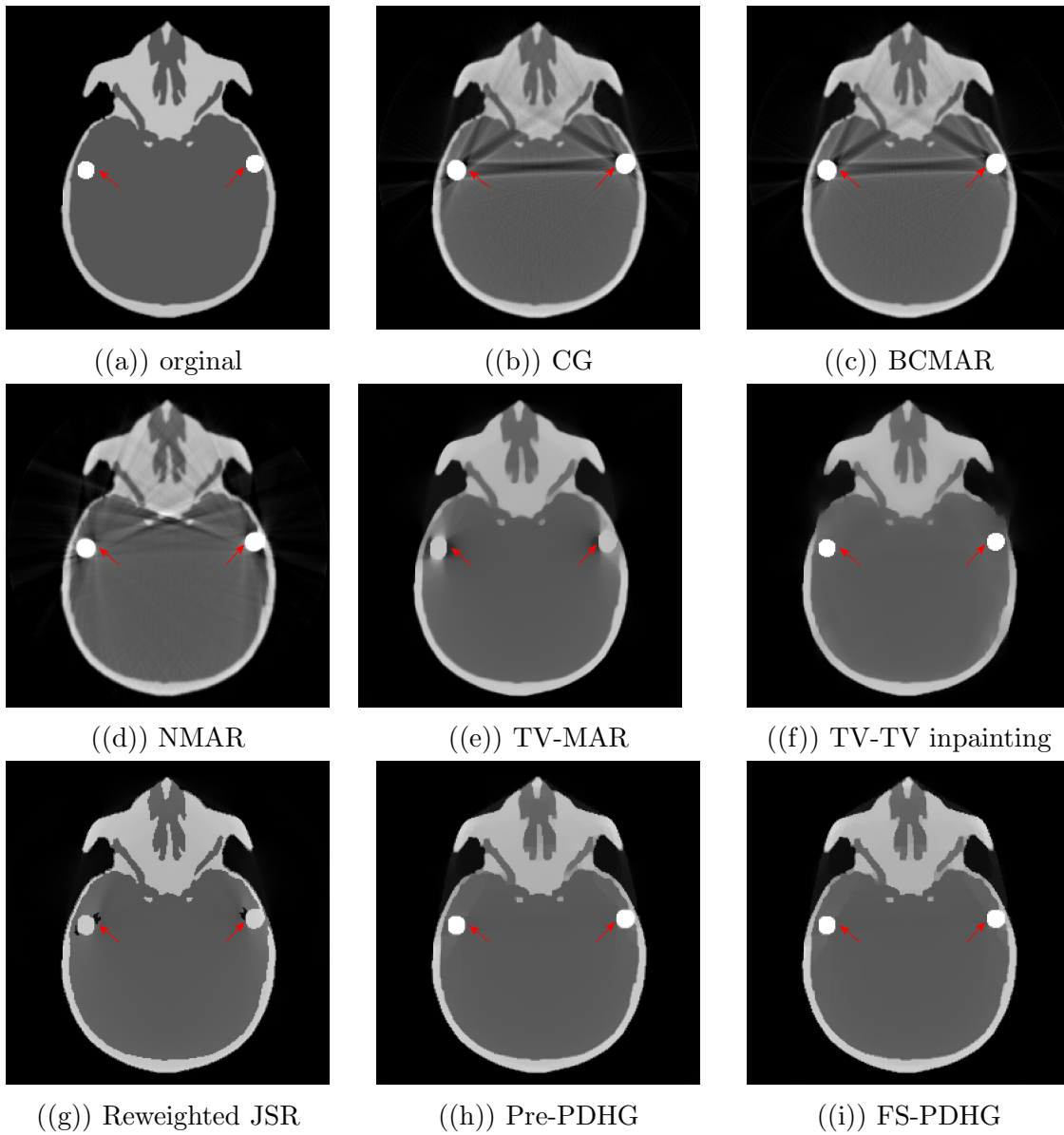


Figure 14: Image reconstruction of the head phantom by ground truth, CG, BCMAR, NMAR, TV-MAR, TV-TV inpainting, Reweighted JSR, Pre-PDHG and FS-PDHG (4200 HU window, 1100 HU level).

proposed FS-PDHG conspicuously curtails computational expenditure, reducing the total computational cost to at most one-third.

5.5 Experiments on real data

To further illustrate the validity, we conducted a CT scan of a tooth enclosed in a plastic bottle with two titanium rods positioned on one side (Figure 17). The projection data are from a microscopic CT scanner independently developed by Capital Normal University. Each projection view comprised 540 angles, with 752 detector bins employed.

Table 2: Reconstruction error, SSIM index, PSNR value, and the CPU time (sec.) for a single image of the NCAT, head and skull phantoms reconstructed by different algorithms, i.e., CG, BCMAR [3], NMAR [13], TV-MAR (using the primal-dual algorithm), TV-TV inpainting [44], Reweighted JSR model [36] and ours.

Model	Reconstruction error	SSIM	PSNR	Time
CG	0.1586	0.7107	26.0206	—
BCMAR	0.1557	0.7124	26.1511	—
NMAR	0.1144	0.8921	28.2581	—
TV-MAR	0.1080	0.9758	28.7206	207
TV-TV inpainting	0.1060	0.9789	28.8581	245
Reweighted JSR	0.0829	0.9831	30.6438	492
Pre-PDHG	0.0839	0.9932	30.8273	438
FS-PDHG	0.0825	0.9947	30.9797	238

((a)) NCAT

Model	Reconstruction error	SSIM	PSNR	Time
CG	0.1530	0.7339	27.8421	—
BCMAR	0.1503	0.7388	28.0049	—
NMAR	0.1308	0.7608	29.0103	—
TV-MAR	0.1332	0.9114	28.6113	164
TV-TV inpainting	0.1217	0.9220	28.9188	355
Reweighted JSR	0.1199	0.9085	29.5254	525
Pre-PDHG	0.1109	0.9470	30.2593	454
FS-PDHG	0.1093	0.9486	30.3540	344

((b)) Head

Model	Reconstruction error	SSIM	PSNR	Time
CG	0.1892	0.8511	29.4922	—
BCMAR	0.1808	0.9394	29.8744	—
NMAR	0.1648	0.8550	30.2571	—
TV-MAR	0.1745	0.9565	29.8293	290
TV-TV inpainting	0.1700	0.9575	29.8788	400
Reweighted JSR	0.1676	0.9500	30.5401	1104
Pre-PDHG	0.1323	0.9675	32.1448	1079
FS-PDHG	0.1299	0.9681	32.2954	388

((c)) Skull

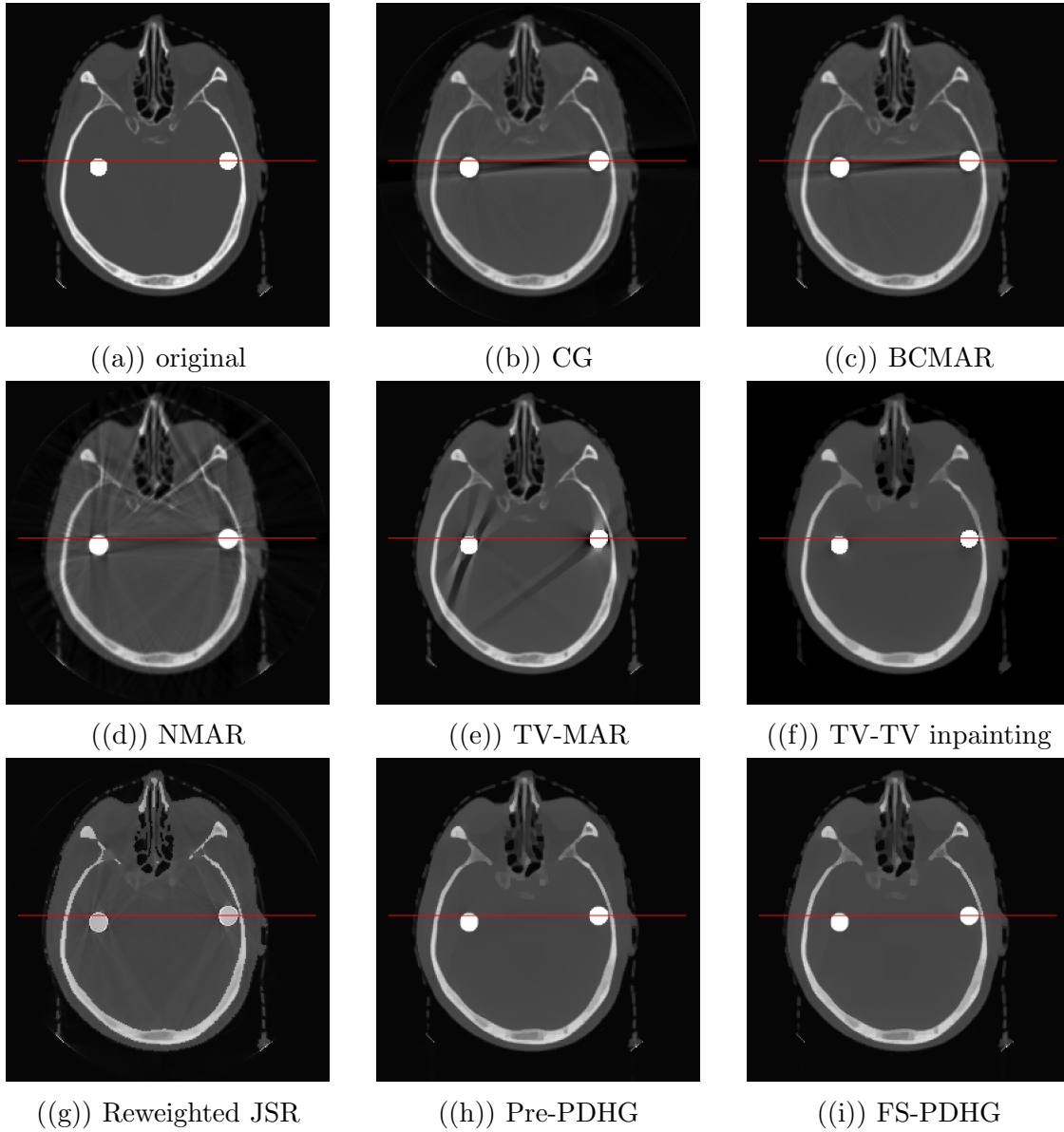


Figure 15: Comparison of numerical simulation results using the skull phantom (2800 HU window, 400 HU level).

The distance from the rotation center to the ray source was 200mm, while the distance from the rotation center to the detector was 890mm. Additionally, the space between each detector bin was set at 0.1mm. The reconstructed image consisted of 256×256 pixels.

Figure 18 displays reconstructed images obtained using various methods, including CG, BCMAR, NMAR, TV-MAR, Reweighted JSR and the proposed FS-PDHG. These images, shown in this section, are presented in the grayscale range of $[0, 0.3]$. NMAR performs better than CG and BCMAR, in preserving image details and correcting artifacts, albeit with the presence of new artifacts near the metal. Furthermore, the results obtained from variation-based models exhibit significantly less noise. Our

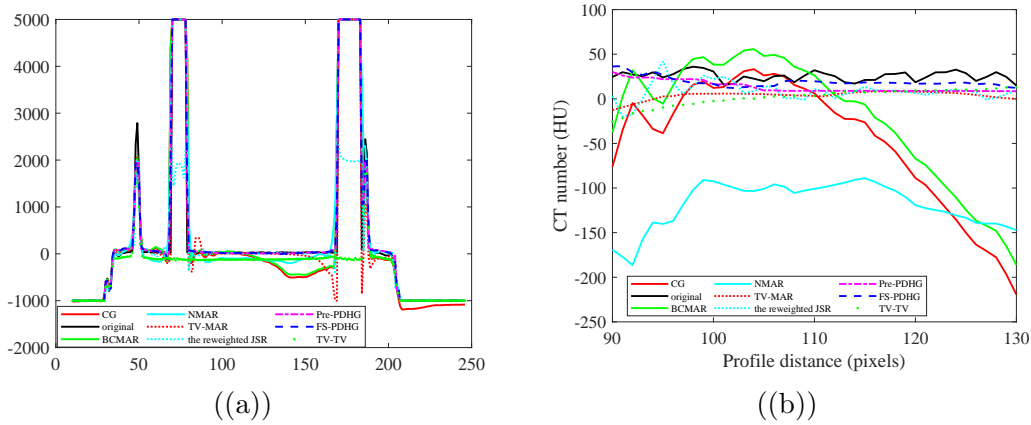


Figure 16: (a) The CT value curve corresponding to the red line representing the MAR results in Figure 15. (b) The local results within the range of [90, 130] in Figure (16(a)).

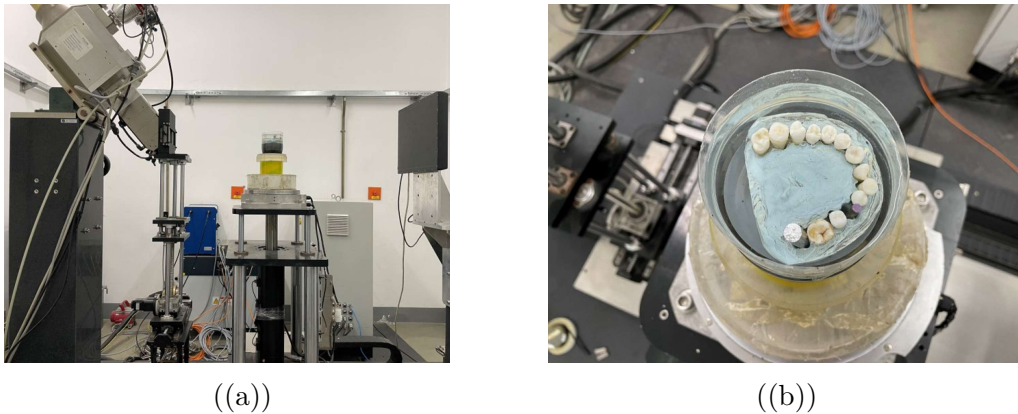


Figure 17: (a) Scanning device. (b) Tooth with metal on one side.

proposed method demonstrates the best overall performance in terms of preserving details and rectifying artifacts, especially near the teeth pointed by red arrows in Figure 18.

6 Conclusions

In this paper, a nonlinear optimization model combining a weighted box-constraint has been proposed for metal artifact removal, whereby non-convex regularization is incorporated into the MAR framework to enhance edge contrast. Instead of directly treating metal trace as missing data, adaptive weights are considered to promote effective reconstruction of projection structures of distinct regions and inhibit diffusion effect, constituting a high-fidelity image reconstruction model. Novel convergent algorithms including preconditioning and full splitting primal-dual algorithms have been developed. To validate the proposed model, both simulated and real experiments have been conducted, demonstrating the superiority of the presented approaches.

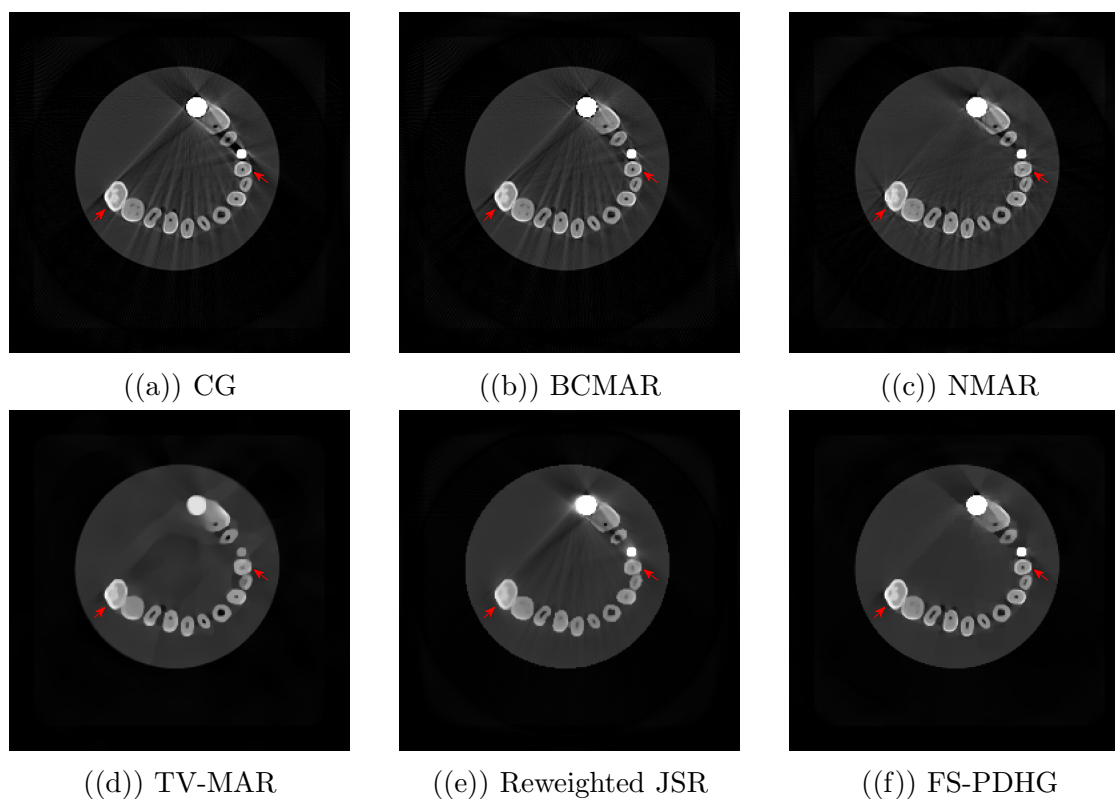


Figure 18: Reconstruction results of the real dental bone (Gray value range $[0, 0.3]$).

Data availability policy

The data that support the findings of this study are available upon request from the authors.

Acknowledgments

The work is partially supported by the National Natural Science Foundation of China (Nos. 12271404, 62201384, 12301545, and 11871372), the Tianjin Research Innovation Project for Postgraduate Students 2022SKY257 and PHD Program 52XB2013 of Tianjin Normal University.

We would like to express our sincere gratitude to the editor and the two reviewers for their invaluable comments, which significantly enhanced the quality of the paper. Additionally, we would like to express our appreciation to Professor Wang Chao from the School of Science, Southern University of Science and Technology for constructive suggestions.

Appendix A Proof of Lemma 4.1

Proof. A direct differentiation calculus gives that

$$\partial L_\lambda(X) = \begin{cases} \partial G(u) - \operatorname{div}(p + \alpha q) + \mathcal{M}_\lambda(u - \tilde{u}), \\ \partial g^*(q) + \alpha \nabla u, \\ -\partial f_\eta^*(p) + \nabla u, \\ \mathcal{M}_\lambda(\tilde{u} - u). \end{cases}$$

Since X^* is a critical point of L_λ , then $0 \in \partial L_\lambda(X^*)$, i.e.

$$\begin{cases} 0 \in \partial G(u^*) - \operatorname{div}(p^* + \alpha q^*) + \mathcal{M}_\lambda(u^* - \tilde{u}^*), \\ 0 \in \partial g^*(q^*) + \alpha \nabla u^*, \\ 0 \in -\partial f_\eta^*(p^*) + \nabla u^*, \\ 0 = \mathcal{M}_\lambda(\tilde{u}^* - u^*). \end{cases}$$

Therefore, $0 \in \partial L_{PD}(u^*, q^*, p^*)$ with positive definite operator \mathcal{M}_λ .

If $\eta = 0$, we conclude that

$$\begin{aligned} \operatorname{div}(p^* + \alpha q^*) &\in \partial G(u^*), \\ \nabla u^* &\in \partial f^*(p^*), \\ -\alpha \nabla u^* &\in \partial g^*(q^*). \end{aligned} \tag{A.1}$$

Due to the closed convex functions f and g , the conclusions hold

$$p^* \in \partial f(\nabla u^*), \quad q^* \in \partial g(-\alpha \nabla u^*).$$

Hence we can deduce that

$$\begin{aligned} 0 &= \operatorname{div}(p^* + \alpha q^*) + \nabla^T p^* + \alpha \nabla^T q^* \\ &\in \partial G(u^*) + \nabla^T [\partial f(\nabla u^*)] - \alpha \nabla^T [\partial g(\nabla u^*)]. \end{aligned} \tag{A.2}$$

Thus we get the desired lemma by (A.2). \square

Appendix B Proof of Lemma 4.2

Proof. First, we consider the subproblem in Step 1 of (3.7) as

$$\begin{aligned} &L_\lambda(X^k) - L_\lambda(u^{k+1}, q^k, p^k, u^{k-1}) \\ (4.7) \quad &\geq \|E_u^{k+1}\|_{\mathcal{M}_\lambda}^2 + \frac{1}{2} \|E_u^k\|_{\mathcal{M}_\lambda}^2 - \frac{\|u^{k+1} - u^{k-1}\|_{\mathcal{M}_\lambda}^2}{2}. \end{aligned} \tag{B.1}$$

For the subproblem in Step 3 of (3.7), similarly, we have

$$\begin{aligned} &L_\lambda(u^{k+1}, q^k, p^k, u^{k-1}) - L_\lambda(u^{k+1}, q^{k+1}, p^k, u^{k-1}) \\ (4.8) \quad &\geq \frac{1}{\tau} \|E_q^{k+1}\|^2 + \alpha \langle \nabla(\bar{u}^{k+1} - u^{k+1}), q^{k+1} - q^k \rangle. \end{aligned} \tag{B.2}$$

For the subproblem in Step 4 of (3.7),

$$\begin{aligned}
& L_\lambda(u^{k+1}, q^{k+1}, p^k, u^{k-1}) - L_\lambda(u^{k+1}, q^{k+1}, p^{k+1}, u^{k-1}) \\
& \stackrel{(4.9)}{\geq} \frac{\|E_p^k\|^2}{2\beta} + \left(\frac{\eta}{2} + \frac{1}{2\beta}\right) \|E_p^{k+1}\|^2 + \langle \nabla(\bar{u}^k - u^{k+1}), p^{k+1} - p^k \rangle \\
& \quad - \frac{\|p^{k+1} - p^{k-1}\|^2}{2\beta} \geq \frac{\eta}{2} \|E_p^{k+1}\|^2 + \langle \nabla(\bar{u}^k - u^{k+1}), p^{k+1} - p^k \rangle.
\end{aligned} \tag{B.3}$$

Moreover,

$$\begin{aligned}
& L_\lambda(u^{k+1}, q^{k+1}, p^{k+1}, u^{k-1}) - L_\lambda(X^{k+1}) \\
& = \frac{\|u^{k+1} - u^{k-1}\|_{\mathcal{M}_\lambda}^2}{2} - \frac{\|E_u^{k+1}\|_{\mathcal{M}_\lambda}^2}{2}.
\end{aligned} \tag{B.4}$$

Summing up (B.1) and (B.4), and using $2ab \leq \xi a^2 + \frac{b^2}{\xi}$, for any $\xi > 0$, it follows

$$\begin{aligned}
& L_\lambda(X^k) - L_\lambda(X^{k+1}) \\
& \geq \langle \nabla(u^k - u^{k+1} + u^k - u^{k-1}), p^{k+1} - p^k \rangle + \frac{1}{\tau} \|E_q^{k+1}\|^2 + \frac{\eta}{2} \|E_p^{k+1}\|^2 \\
& \quad + \alpha \langle \nabla(u^{k+1} - u^k), q^{k+1} - q^k \rangle + \frac{\|E_u^{k+1}\|_{\mathcal{M}_\lambda}^2}{2} + \frac{\|E_u^k\|_{\mathcal{M}_\lambda}^2}{2} \\
& \geq \left(\frac{2}{\tau} - K\alpha\right) \frac{\|E_q^{k+1}\|^2}{2} + (\eta - 2K\xi_1) \frac{\|E_p^{k+1}\|^2}{2} + \frac{\|E_u^k\|_{\mathcal{M}_\lambda - \frac{K}{\xi_1}\mathcal{I}}^2}{2} \\
& \quad + \frac{\|E_u^{k+1}\|_{\mathcal{M}_\lambda - (\frac{K}{\xi_1} + K\alpha)\mathcal{I}}^2}{2}
\end{aligned} \tag{B.5}$$

with $\xi_1 < \frac{\eta}{2K}$. Due to Condition 1, the operator $\mathcal{M}_\lambda - (\frac{K}{\xi_1} + K\alpha)\mathcal{I}$ is positive definite, such that $\|E_u^{k+1}\|_{\mathcal{M}_\lambda - (\frac{K}{\xi_1} + K\alpha)\mathcal{I}}^2 \geq C_1 \|E_u^{k+1}\|^2$ with the minimum eigenvalue C_1 .

Rearranging the above equation gives the desired Lemma. \square

Appendix C Proof of Lemma 4.3

Proof. Obviously, the sequence $\{X^k\}$ is bounded. One can readily prove the nonincrease of (4.3) by Lemma 4.2, and

$$\begin{aligned}
& L_\lambda(X^k) \\
& = G(u^k) + g^*(q^k) - f_\eta^*(p^k) + \langle \nabla u^k, p^k + \alpha q^k \rangle + \frac{\|E_u^k\|_{\mathcal{M}_\lambda}^2}{2} \\
& \leq G(u^0) + g^*(q^0) - f_\eta^*(p^0) + \langle \nabla u^0, p^0 + \alpha q^0 \rangle,
\end{aligned} \tag{C.1}$$

where we have introduced $u^{-1} = u^0$.

On the other hand,

$$\begin{aligned}
& L_\lambda(X^k) \\
&= G(u^k) + g^*(q^k) - f_\eta^*(p^k) + \langle \nabla u^k, p^k + \alpha q^k \rangle + \frac{\|E_u^k\|_{\mathcal{M}_\lambda}^2}{2} \\
&\geq G(u^k) + g^*(q^k) - f_\eta^*(p^k) + \frac{\|E_u^k\|_{\mathcal{M}_\lambda}^2}{2} - \frac{K\alpha\|u^k\|^2}{2} + \frac{\|Kp^k + \alpha q^k\|^2}{2\alpha} \\
&\geq G(u^k) + g^*(q^k) - f^*(p^k) - \frac{\eta}{2} + \frac{\|E_u^k\|_{\mathcal{M}_\lambda}^2}{2} - \frac{Kc^2\alpha + K(1+\alpha)^2}{2\alpha} \\
&> -\infty.
\end{aligned}$$

□

Appendix D Proof of Lemma 4.4

Proof. We first estimate the upper bound of the partial derivative w.r.t. to u . By (4.4),

$$\operatorname{div}(p^k - p^{k+1}) + \alpha \operatorname{div}(q^k - q^{k+1}) \in \partial_u L_\lambda(X^{k+1}).$$

Hence we need to estimate the bound of the left-hand-side term of the above equation. Readily

$$\operatorname{dist}(0, \partial_u L_\lambda(X^{k+1})) \leq K\|E_p^{k+1}\| + K\alpha\|E_q^{k+1}\|. \quad (\text{D.1})$$

Then consider the derivative w.r.t. q . Similarly,

$$\begin{aligned}
& \alpha(\nabla u^{k+1} - \nabla \bar{u}^{k+1}) + \frac{q^k - q^{k+1}}{\tau} \\
&= \alpha \nabla(u^k - u^{k+1}) + \frac{q^k - q^{k+1}}{\tau} \in \partial_q L_\lambda(X^{k+1}).
\end{aligned}$$

We have

$$\operatorname{dist}(0, \partial_q L_\lambda(X^{k+1})) \leq K\alpha\|E_u^{k+1}\| + \frac{1}{\tau}\|E_q^{k+1}\|. \quad (\text{D.2})$$

For the derivative w.r.t. p ,

$$\begin{aligned}
& \nabla u^{k+1} - \nabla \bar{u}^{k+1} - \frac{p^k - p^{k+1}}{\beta} \\
&= \nabla(u^k - u^{k+1}) - \frac{p^k - p^{k+1}}{\beta} \in \partial_p L_\lambda(X^{k+1}).
\end{aligned}$$

Then

$$\operatorname{dist}(0, \partial_p L_\lambda(X^{k+1})) \leq K\|E_u^{k+1}\| + \frac{1}{\beta}\|E_p^{k+1}\|. \quad (\text{D.3})$$

Last we consider w.r.t. \tilde{u}

$$\operatorname{dist}(0, \nabla_{\tilde{u}} L_\sigma(X^{k+1})) = \|\mathcal{M}_\lambda(u^{k+1} - u^k)\| \leq \|\mathcal{M}_\lambda\| \|E_u^{k+1}\|. \quad (\text{D.4})$$

Since

$$\begin{aligned} \text{dist}(0, \partial L_\lambda(X^{k+1})) &\leq \text{dist}(0, \partial_u L_\lambda(X^{k+1})) + \text{dist}(0, \partial_q L_\lambda(X^{k+1})) \\ &\quad + \text{dist}(0, \partial_p L_\lambda(X^{k+1})) + \text{dist}(0, \nabla_{\tilde{u}} L_\lambda(X^{k+1})), \end{aligned}$$

we finally conclude Lemma 4.4 with the given C_2 by summing up (D.1)-(D.4). \square

Appendix E Proof of Lemma 4.5

Proof. Similar to the proof of Lemma 4.1, if $Z^* = (\Lambda^*, u^*, v^*, q^*, p^*, \tilde{u}^*, \tilde{v}^*)$ is a critical point of the function L_σ , $(u^*, v^*, q^*, p^*, \Lambda^*)$ is a critical point of L . Therefore details are omitted here.

At the same time, we have

$$\begin{cases} 0 \in \partial h(u^*) - \mathcal{P}^T \Lambda^* - \text{div}(p^* + \alpha q^*), \\ 0 = \nabla F(v^*) + \Lambda^*, \\ 0 \in \partial g^*(q^*) + \alpha \nabla u^*, \\ 0 \in -\partial f_\eta^*(p^*) + \nabla u^*, \\ 0 = v^* - \mathcal{P}u^*. \end{cases}$$

Owing to $\eta = 0$, we can obtain by closed convex functions f and g

$$p^* \in \partial f(\nabla u^*), \quad q^* \in \partial g(-\alpha \nabla u^*).$$

Meanwhile,

$$\nabla F(v^*) = \frac{1}{\lambda} (W \odot W \odot (v^* - Y)) = \frac{1}{\lambda} (W \odot W \odot (\mathcal{P}u^* - Y)).$$

We further derive that

$$\begin{aligned} 0 &= \text{div}(p^* + \alpha q^*) + \nabla^T p^* + \alpha \nabla^T q^* \\ &= \frac{1}{\lambda} \mathcal{P}^T (W \odot W \odot (\mathcal{P}u^* - Y)) + \partial h(u^*) \\ &\quad + \nabla^T [\partial f(\nabla u^*)] - \alpha \nabla^T [\partial g(\nabla u^*)]. \end{aligned} \tag{E.1}$$

Consequently, we get the desired lemma by (E.1). \square

Appendix F Proof of Lemma 4.6

Due to the subproblems of (3.13), the following relations hold:

$$\text{div}(p^k + \alpha q^k) + \mathcal{P}^T \Lambda^{k+1} + \frac{u^k - u^{k+1}}{\sigma_1} \in \partial h(u^{k+1}), \tag{F.1}$$

$$-\Lambda^{k+1} + \frac{v^k - v^{k+1}}{\sigma_2} = \nabla F(v^{k+1}), \tag{F.2}$$

$$\Lambda^{k+1} - \Lambda^k = \rho(v^k - \mathcal{P}u^k). \tag{F.3}$$

Note that the subproblems about q and p are same as Algorithm 1, and we omit them.

Proof. Due to the subproblems with strongly convex property, we get the following estimate:

$$h(u^k) - h(u^{k+1}) \geq \langle \operatorname{div}(p^k + \alpha q^k) + \mathcal{P}^T \Lambda^{k+1}, u^k - u^{k+1} \rangle + \frac{1}{\sigma_1} \|E_u^{k+1}\|^2, \quad (\text{F.4})$$

$$F(v^k) - F(v^{k+1}) \geq -\langle \Lambda^{k+1}, v^k - v^{k+1} \rangle + \frac{\|v^k - v^{k+1}\|^2}{\sigma_2}. \quad (\text{F.5})$$

First, we consider the subproblem in Step 1 of (3.13) as

$$\begin{aligned} L_\sigma(Z^k) - L_\sigma(\Lambda^{k+1}, u^k, v^k, q^k, p^k, u^{k-1}, v^{k-1}) \\ = \langle \Lambda^k - \Lambda^{k+1}, v^k - P u^k \rangle = -\frac{1}{\rho} \|E_\Lambda^{k+1}\|^2 \end{aligned} \quad (\text{F.6})$$

By (F.2), we have

$$\begin{aligned} & \|E_\Lambda^{k+1}\|^2 \\ &= \left\| \nabla F(v^k) - \nabla F(v^{k+1}) + \frac{v^k - v^{k+1}}{\sigma_2} - \frac{v^{k-1} - v^k}{\sigma_2} \right\|^2 \\ &\leq 2 \left\| \nabla F(v^k) - \nabla F(v^{k+1}) + \frac{v^k - v^{k+1}}{\sigma_2} \right\|^2 + \frac{2}{\sigma_2^2} \|E_v^k\|^2 \\ &\leq 4 \left\| \nabla F(v^k) - \nabla F(v^{k+1}) \right\|^2 + \frac{4}{\sigma_2^2} \|E_v^{k+1}\|^2 + \frac{2}{\sigma_2^2} \|E_v^k\|^2 \\ &\leq 4 \left(\frac{1}{\lambda^2} \|W\|_{\max}^4 + \frac{1}{\sigma_2^2} \right) \|E_v^{k+1}\|^2 + \frac{2}{\sigma_2^2} \|E_v^k\|^2. \end{aligned} \quad (\text{F.7})$$

Then we estimate the subproblem in Step 2 of (3.13) as

$$\begin{aligned} L_\sigma(\Lambda^{k+1}, u^k, v^k, q^k, p^k, u^{k-1}, v^{k-1}) - L_\sigma(\Lambda^{k+1}, u^{k+1}, v^k, q^k, p^k, u^k, v^{k-1}) \\ \geq \frac{1}{2\sigma_1} \|E_u^{k+1}\|^2 + \frac{1}{2\sigma_1} \|E_u^k\|^2. \end{aligned} \quad (\text{F.8})$$

For the subproblem in Step 4 of (3.13), similarly, we have

$$\begin{aligned} L_\sigma(\Lambda^{k+1}, u^{k+1}, v^k, q^k, p^k, u^k, v^{k-1}) - L_\sigma(\Lambda^{k+1}, u^{k+1}, v^{k+1}, q^k, p^k, u^k, v^k) \\ \geq \frac{1}{2\sigma_2} \|E_v^{k+1}\|^2 + \frac{1}{2\sigma_2} \|E_v^k\|^2. \end{aligned} \quad (\text{F.9})$$

Regarding the subproblems of q and p , (B.2) and (B.3) give

$$\begin{aligned} L_\sigma(\Lambda^{k+1}, u^{k+1}, v^{k+1}, q^k, p^k, u^k, v^k) - L_\sigma(\Lambda^{k+1}, u^{k+1}, v^{k+1}, q^{k+1}, p^k, u^k, v^k) \\ \geq \frac{1}{\tau} \|E_q^{k+1}\|^2 + \alpha \langle \nabla u^{k+1} - \nabla u^k, q^{k+1} - q^k \rangle, \\ L_\sigma(\Lambda^{k+1}, u^{k+1}, v^{k+1}, q^{k+1}, p^k, u^k, v^k) - L_\sigma(Z^{k+1}) \\ \geq \frac{\eta}{2} \|E_p^{k+1}\|^2 + \langle \nabla(u^{k+1} - u^k + u^k - u^{k+1}), p^{k+1} - p^k \rangle. \end{aligned} \quad (\text{F.10})$$

Summing up (F.6) and (F.10), it follows

$$\begin{aligned}
& L_\sigma(Z^k) - L_\sigma(Z^{k+1}) \\
& \geq \left(1 - \frac{K\sigma_1}{\xi_2}\right) \frac{\|E_u^{k+1}\|^2 + \|E_u^k\|^2}{2\sigma_1} + \left(\frac{2}{\tau} - K\alpha\right) \frac{\|E_q^{k+1}\|^2}{2} \\
& \quad - K\alpha \frac{\|E_u^{k+1}\|^2}{2} + (\eta - 2K\xi_2) \frac{\|E_p^{k+1}\|^2}{2} + \left(\frac{1}{2\sigma_2} - \frac{2}{\rho\sigma_2^2}\right) \|E_v^k\|^2 \\
& \quad + \left(\frac{1}{2\sigma_2} - \frac{4}{\rho} \left(\frac{1}{\lambda^2} \|W\|_{\max}^4 + \frac{1}{\sigma_2^2}\right)\right) \|E_v^{k+1}\|^2.
\end{aligned} \tag{F.11}$$

Rearranging the above equation and setting

$$\tilde{C} := \min \left\{ \frac{1}{2\sigma_1} - \frac{K}{2\xi_2} - \frac{K\alpha}{2}, \frac{1}{\tau} - \frac{K\alpha}{2}, \frac{\eta}{2} - K\xi_2, \right. \\
\left. \frac{1}{2\sigma_2} - 4 \left(\frac{1}{\lambda^2} \|W\|_{\max}^4 + \frac{1}{\sigma_2^2} \right) \right\},$$

readily we obtain

$$L_\sigma(Z^k) - L_\sigma(Z^{k+1}) \geq \tilde{C} \|Z^{k+1} - Z^k\|^2.$$

□

References

- [1] A. Katsevich, “Theoretically exact filtered backprojection-type inversion algorithm for spiral CT,” *SIAM Journal on Applied Mathematics*, vol. 62, no. 6, pp. 2012–2026, 2002.
- [2] A. H. Andersen and A. C. Kak, “Simultaneous algebraic reconstruction technique (SART): a superior implementation of the ART algorithm,” *Ultrasonic imaging*, vol. 6, no. 1, pp. 81–94, 1984.
- [3] H. S. Park, D. Hwang, and J. K. Seo, “Metal artifact reduction for polychromatic X-ray CT based on a beam-hardening corrector,” *IEEE transactions on medical imaging*, vol. 35, no. 2, pp. 480–487, 2015.
- [4] S. M. Lee, T. Bayaraa, H. Jeong, C. M. Hyun, and J. K. Seo, “A direct sinogram correction method to reduce metal-related beam-hardening in computed tomography,” *IEEE Access*, vol. 7, pp. 128 828–128 836, 2019.
- [5] J. Hur, D. Kim, Y.-G. Shin, and H. Lee, “Metal artifact reduction method based on a constrained beam-hardening estimator for polychromatic X-ray CT,” *Physics in Medicine and Biology*, vol. 66, no. 6, p. 065025, 2021.
- [6] M. A. Hegazy, M. H. Cho, M. H. Cho, and S. Y. Lee, “Metal artifact reduction in dental CBCT images using direct sinogram correction combined with metal path-length weighting,” *Sensors*, vol. 23, no. 3, p. 1288, 2023.
- [7] M. Zhu, Q. Zhu, Y. Song, Y. Guo, D. Zeng, Z. Bian, Y. Wang, and J. Ma, “Physics-informed sinogram completion for metal artifact reduction in CT imaging,” *Physics in Medicine and Biology*, vol. 68, no. 6, p. 065006, 2023.
- [8] W. A. Kalender, R. Hebel, and J. Ebersberger, “Reduction of CT artifacts caused by metallic implants,” *Radiology*, vol. 164, no. 2, pp. 576–577, 1987.
- [9] P. P. Bruyant, J. Sau, and J.-J. Mallet, “Streak artifact reduction in filtered backprojection using a level line-based interpolation method,” *Journal of Nuclear Medicine*, vol. 41, no. 11, pp. 1913–1919, 2000.

- [10] J. C. Roeske, C. Lund, C. A. Pelizzari, X. Pan, and A. J. Mundt, "Reduction of computed tomography metal artifacts due to the fletcher-suit applicator in gynecology patients receiving intracavitary brachytherapy," *Brachytherapy*, vol. 2, no. 4, pp. 207–214, 2003.
- [11] J.-w. Gu, L. Zhang, Z.-q. Chen, Y.-x. Xing, and Z.-f. Huang, "A method based on interpolation for metal artifacts reduction in CT images," *Journal of X-ray Science and Technology*, vol. 14, no. 1, pp. 11–19, 2006.
- [12] W. J. Veldkamp, R. M. Joemai, A. J. van der Molen, and J. Geleijns, "Development and validation of segmentation and interpolation techniques in sinograms for metal artifact suppression in CT," *Medical physics*, vol. 37, no. 2, pp. 620–628, 2010.
- [13] E. Meyer, R. Raupach, M. Lell, B. Schmidt, and M. Kachelrieß, "Normalized metal artifact reduction (NMAR) in computed tomography," *Medical physics*, vol. 37, no. 10, pp. 5482–5493, 2010.
- [14] M. Axente, A. Paidi, R. Von Eyben, C. Zeng, A. Bani-Hashemi, A. Krauss, and D. Hristov, "Clinical evaluation of the iterative metal artifact reduction algorithm for ct simulation in radiotherapy," *Medical physics*, vol. 42, no. 3, pp. 1170–1183, 2015.
- [15] X. Huang, J. Wang, F. Tang, T. Zhong, and Y. Zhang, "Metal artifact reduction on cervical CT images by deep residual learning," *Biomedical engineering online*, vol. 17, pp. 1–15, 2018.
- [16] H. Liao, W.-A. Lin, S. K. Zhou, and J. Luo, "ADN: artifact disentanglement network for unsupervised metal artifact reduction," *IEEE Transactions on Medical Imaging*, vol. 39, no. 3, pp. 634–643, 2019.
- [17] L. Gjestebj, H. Shan, Q. Yang, Y. Xi, Y. Jin, D. Giantsoudi, H. Paganetti, B. De Man, and G. Wang, "A dual-stream deep convolutional network for reducing metal streak artifacts in CT images," *Physics in Medicine and Biology*, vol. 64, no. 23, p. 235003, 2019.
- [18] J. S. Nielsen, J. M. Edmund, and K. Van Leemput, "Magnetic resonance-based computed tomography metal artifact reduction using bayesian modelling," *Physics in Medicine and Biology*, vol. 64, no. 24, p. 245012, 2019.
- [19] G. Li, L. Ji, C. You, S. Gao, L. Zhou, K. Bai, S. Luo, and N. Gu, "Marganvac: metal artifact reduction method based on generative adversarial network with variable constraints," *Physics in Medicine and Biology*, vol. 68, no. 20, p. 205005, 2023.
- [20] L. Gjestebj, Q. Yang, Y. Xi, Y. Zhou, J. Zhang, and G. Wang, "Deep learning methods to guide CT image reconstruction and reduce metal artifacts," in *Medical Imaging 2017: Physics of Medical Imaging*, vol. 10132. SPIE, 2017, pp. 752–758.
- [21] Y. Zhang and H. Yu, "Convolutional neural network based metal artifact reduction in X-ray computed tomography," *IEEE transactions on medical imaging*, vol. 37, no. 6, pp. 1370–1381, 2018.
- [22] M. U. Ghani and W. C. Karl, "Fast enhanced CT metal artifact reduction using data domain deep learning," *IEEE Transactions on Computational Imaging*, vol. 6, pp. 181–193, 2019.
- [23] L. Yu, Z. Zhang, X. Li, and L. Xing, "Deep sinogram completion with image prior for metal artifact reduction in CT images," *IEEE transactions on medical imaging*, vol. 40, no. 1, pp. 228–238, 2020.
- [24] P. Trapp, J. Maier, M. Susenburger, S. Sawall, and M. Kachelrieß, "Empirical scatter correction: CBCT scatter artifact reduction without prior information," *Medical Physics*, vol. 49, no. 7, pp. 4566–4584, 2022.
- [25] Y. Lyu, W.-A. Lin, H. Liao, J. Lu, and S. K. Zhou, "Encoding metal mask projection for metal artifact reduction in computed tomography," in *Medical Image Computing and Computer Assisted Intervention—MICCAI 2020: 23rd International Conference, Lima, Peru, October 4–8, 2020, Proceedings, Part II 23*. Springer, 2020, pp. 147–157.
- [26] M. Ikuta and J. Zhang, "A deep recurrent neural network with fista optimization for ct metal artifact reduction," *IEEE Transactions on Computational Imaging*, vol. 8, pp. 961–971, 2022.
- [27] B. Zhou, X. Chen, S. K. Zhou, J. S. Duncan, and C. Liu, "DuDoDR-Net: Dual-domain data consistent recurrent network for simultaneous sparse view and metal artifact reduction in

- computed tomography,” *Medical Image Analysis*, vol. 75, p. 102289, 2022.
- [28] C. M. Hyun, T. Bayaraa, H. S. Yun, T.-J. Jang, H. S. Park, and J. K. Seo, “Deep learning method for reducing metal artifacts in dental cone-beam CT using supplementary information from intra-oral scan,” *Physics in Medicine and Biology*, vol. 67, no. 17, p. 175007, 2022.
- [29] H. Wang, Y. Li, H. Zhang, D. Meng, and Y. Zheng, “InDuDoNet+: A deep unfolding dual domain network for metal artifact reduction in CT images,” *Medical Image Analysis*, vol. 85, p. 102729, 2023.
- [30] E. Y. Sidky and X. Pan, “Image reconstruction in circular cone-beam computed tomography by constrained, total-variation minimization,” *Physics in Medicine and Biology*, vol. 53, no. 17, p. 4777, 2008.
- [31] L. Ritschl, F. Bergner, C. Fleischmann, and M. Kachelrieß, “Improved total variation-based CT image reconstruction applied to clinical data,” *Physics in Medicine and Biology*, vol. 56, no. 6, p. 1545, 2011.
- [32] Z. Chen, X. Jin, L. Li, and G. Wang, “A limited-angle CT reconstruction method based on anisotropic TV minimization,” *Physics in Medicine and Biology*, vol. 58, no. 7, p. 2119, 2013.
- [33] H. Zhang, L. Wang, L. Li, A. Cai, G. Hu, and B. Yan, “Iterative metal artifact reduction for x-ray computed tomography using unmatched projector backprojector pairs,” *Medical physics*, vol. 43, no. 6, pp. 3019–3033, 2016.
- [34] B. Dong, J. Li, and Z. Shen, “X-ray CT image reconstruction via wavelet frame based regularization and Radon domain inpainting,” *Journal of Scientific Computing*, vol. 54, pp. 333–349, 2013.
- [35] R. Zhan and B. Dong, “CT image reconstruction by spatial-radon domain data-driven tight frame regularization,” *SIAM Journal on Imaging Sciences*, vol. 9, no. 3, pp. 1063–1083, 2016.
- [36] H. Zhang, B. Dong, and B. Liu, “A reweighted joint spatial-radon domain CT image reconstruction model for metal artifact reduction,” *SIAM Journal on Imaging Sciences*, vol. 11, no. 1, pp. 707–733, 2018.
- [37] J. K. Choi, C. Bao, and X. Zhang, “PET-MRI joint reconstruction by joint sparsity based tight frame regularization,” *SIAM Journal on Imaging Sciences*, vol. 11, no. 2, pp. 1179–1204, 2018.
- [38] Y. Liu, J. Ma, Y. Fan, and Z. Liang, “Adaptive-weighted total variation minimization for sparse data toward low-dose X-ray computed tomography image reconstruction,” *Physics in Medicine and Biology*, vol. 57, no. 23, p. 7923, 2012.
- [39] Y. Lou, T. Zeng, S. Osher, and J. Xin, “A weighted difference of anisotropic and isotropic total variation model for image processing,” *SIAM Journal on Imaging Sciences*, vol. 8, no. 3, pp. 1798–1823, 2015.
- [40] E. Faggiano, T. Lorenzi, and A. Quarteroni, “Metal artefact reduction in computed tomography images by a fourth-order total variation flow,” *Computer Methods in Biomechanics and Biomedical Engineering: Imaging and Visualization*, vol. 4, no. 3-4, pp. 202–213, 2016.
- [41] C. Gong and L. Zeng, “Adaptive iterative reconstruction based on relative total variation for low-intensity computed tomography,” *Signal Processing*, vol. 165, pp. 149–162, 2019.
- [42] Z. Deng, Y. Zhou, W. Zhang, Z. Lin, and J. Zhao, “Customized total variation algorithm for metal artifact reduction in computed tomography,” in *2021 43rd Annual International Conference of the IEEE Engineering in Medicine and Biology Society (EMBC)*. IEEE, 2021, pp. 3479–3482.
- [43] A. Mehranian, M. R. Ay, A. Rahmim, and H. Zaidi, “X-ray CT metal artifact reduction using wavelet domain L_0 sparse regularization,” *IEEE transactions on medical imaging*, vol. 32, no. 9, pp. 1707–1722, 2013.
- [44] H. Zhang, L. Li, L. Wang, Y. Sun, B. Yan, A. Cai, and G. Hu, “Computed tomography sinogram inpainting with compound prior modelling both sinogram and image sparsity,” *IEEE Transactions on Nuclear Science*, vol. 63, no. 5, pp. 2567–2576, 2016.
- [45] C. Wu, Z. Liu, and S. Wen, “A general truncated regularization framework for contrast-preserving variational signal and image restoration: motivation and implementation,” *Science China Mathematics*, vol. 61, pp. 1711–1732, 2018.
- [46] C. Li, R. Huang, Z. Ding, J. C. Gatenby, D. N. Metaxas, and J. C. Gore, “A level set method

- for image segmentation in the presence of intensity inhomogeneities with application to MRI,” *IEEE transactions on image processing*, vol. 20, no. 7, pp. 2007–2016, 2011.
- [47] M. Pragliola, L. Calatroni, A. Lanza, and F. Sgallari, “On and beyond total variation regularization in imaging: The role of space variance,” *SIAM Review*, vol. 65, no. 3, pp. 601–685, 2023.
- [48] F. Park, Y. Lou, and J. Xin, “A weighted difference of anisotropic and isotropic total variation for relaxed mumford-shah image segmentation,” in *2016 IEEE International Conference on Image Processing (ICIP)*. IEEE, 2016, pp. 4314–4318.
- [49] C. Wang, M. Tao, J. G. Nagy, and Y. Lou, “Limited-angle CT reconstruction via the L_1/L_2 minimization,” *SIAM Journal on Imaging Sciences*, vol. 14, no. 2, pp. 749–777, 2021.
- [50] A. C. Kak and M. Slaney, *Principles of computerized tomographic imaging*. SIAM, 2001.
- [51] R. H. Chan and J. Ma, “A multiplicative iterative algorithm for box-constrained penalized likelihood image restoration,” *IEEE transactions on image processing*, vol. 21, no. 7, pp. 3168–3181, 2012.
- [52] K. Kan, S. W. Fung, and L. Ruthotto, “PNKH-B: A projected Newton-Krylov method for large-scale bound-constrained optimization,” *SIAM Journal on Scientific Computing*, vol. 43, no. 5, pp. S704–S726, 2021.
- [53] Y. Lou and M. Yan, “Fast $L_1 - L_2$ minimization via a proximal operator,” *Journal of Scientific Computing*, vol. 74, no. 2, pp. 767–785, 2018.
- [54] T. Goldstein and S. Osher, “The split bregman method for L_1 -regularized problems,” *SIAM journal on imaging sciences*, vol. 2, no. 2, pp. 323–343, 2009.
- [55] M. Zhu and T. Chan, “An efficient primal-dual hybrid gradient algorithm for total variation image restoration,” *Ucla Cam Report*, vol. 34, pp. 8–34, 2008.
- [56] E. Esser, X. Zhang, and T. F. Chan, “A general framework for a class of first order primal-dual algorithms for convex optimization in imaging science,” *SIAM Journal on Imaging Sciences*, vol. 3, no. 4, pp. 1015–1046, 2010.
- [57] A. Chambolle and T. Pock, “A first-order primal-dual algorithm for convex problems with applications to imaging,” *Journal of mathematical imaging and vision*, vol. 40, pp. 120–145, 2011.
- [58] T. Pock and A. Chambolle, “Diagonal preconditioning for first order primal-dual algorithms in convex optimization,” in *2011 International Conference on Computer Vision*. IEEE, 2011, pp. 1762–1769.
- [59] H. Attouch, J. Bolte, P. Redont, and A. Soubeyran, “Proximal alternating minimization and projection methods for nonconvex problems: An approach based on the kurdyka-Lojasiewicz inequality,” *Mathematics of operations research*, vol. 35, no. 2, pp. 438–457, 2010.
- [60] Y. Wang, W. Yin, and J. Zeng, “Global convergence of ADMM in nonconvex nonsmooth optimization,” *Journal of Scientific Computing*, vol. 78, pp. 29–63, 2019.
- [61] R. T. Rockafellar and R. J.-B. Wets, *Variational analysis*. Springer Science and Business Media, 2009, vol. 317.
- [62] Y. Xu and W. Yin, “A block coordinate descent method for regularized multiconvex optimization with applications to nonnegative tensor factorization and completion,” *SIAM Journal on imaging sciences*, vol. 6, no. 3, pp. 1758–1789, 2013.
- [63] J. H. Hubbell and S. M. Seltzer, “Tables of X-ray mass attenuation coefficients and mass energy-absorption coefficients 1 keV to 20 MeV for elements $Z = 1$ to 92 and 48 additional substances of dosimetric interest,” National Inst. of Standards and Technology-PL, Gaithersburg, MD (United . . . , Tech. Rep., 1995.
- [64] Beer, “Bestimmung der absorption des rothen lichts in farbigen flüssigkeiten,” *Annalen der Physik*, vol. 162, no. 5, pp. 78–88, 1852.